Arc crust formation of Lesser Antilles revealed by crustal xenoliths from Petit St. Vincent

Journal Item

Arc crust formation of Lesser Antilles revealed by crustal xenoliths from Petit St. Vincent

Elena Melekhova[1*], Michal Camejo-Harry[2], Jon Blundy[1], Simon R. Wallis[3], Catherine Annen[4], Barbara E. Kunz[5], Frances E. Jenner[5] and Matthew Thirlwall[6]

[1] Department of Earth Sciences, University of Oxford, South Parks Road, Oxford, OX1 3AN, UK
[2] The University of the West Indies Seismic Research Centre, St. Augustine, Trinidad and Tobago
[3] Department of Earth and Planetary Science, School of Science, The University of Tokyo, 7-3-1 Hongo, Bunkyo-ku, Tokyo 113-0033, Japan
[4] Institute of Geophysics, Czech Academy of Sciences, Boční II 1401,141 31 Prague 4, Czech Republic
[5] School of Environment, Earth and Ecosystem Sciences, The Open University, Walton Hall, Milton Keynes, Buckinghamshire MK7 6AA, UK
[6] Department of Earth Sciences, Royal Holloway University of London, Egham, Surrey, TW20 0EX

*elena.melekhova@earth.ox.ac.uk

Key words: crustal xenoliths, arc magmatism, partial melting, arc crust, crust reworking

ABSTRACT

The Lesser Antilles volcanic arc is known for its magmatic diversity and unusually abundant plutonic xenoliths. Xenoliths from Petit St. Vincent (Grenadines archipelago) are particularly interesting because of their textural and petrogenetic range. Here we combine petrographic observations, Electron Backscatter Diffraction (EBSD) analysis, major and trace element chemistry of xenoliths and lavas, and geochemical and thermal modelling to explore the construction of arc crust beneath Petit St. Vincent.

Petit St. Vincent xenoliths are dominated by calcic plagioclase, clinopyroxene and amphibole, and can be divided into two main categories, igneous and meta-igneous. Igneous xenoliths typically have cumulate textures; meta-igneous xenoliths range texturally from those that preserve vestiges of primary magmatic fabrics to intensely deformed varieties characterised by grain-size reduction and foliation development. Meta-igneous xenoliths also contain the most calcic plagioclase (An_{98-100}).

The presence of both meta-igneous and igneous xenoliths provides evidence for reworking of older arc crust and antecedent igneous intrusions. The latter have a protolith composition similar to high-MgO, low-Sr picrites and high-Ca, high-Sr ankaramites from the neighbouring islands of Petite Martinique and Grenada. The meta-igneous xenoliths derive from older, mafic arc crust present at the onset of subduction. Trace element chemistry and EBSD analyses of meta-igneous xenoliths are consistent with a complex history of re-melting and deformation mediated by chlorine-bearing H_2O rich fluids (including melts). Thermal modelling supports crustal reworking through repeated magma intrusions, and indicates that the observed thermal structure and thickness of crust beneath Petit St. Vincent could have developed on a timescale of approximately 4 million years at rates compatible with the regional arc magma flux. Based on evidence from thermodynamic models and exhumed ancient arc crust sections, Collins *et al.* (2020) have proposed that water-fluxed melting may

be an important aspect of deep arc crust sections world-wide. Textures and mineralogy of xenoliths from Petit St Vincent, including their characteristic high-An plagioclase, testify to such a process beneath an active, intra-oceanic arc.

HIGHLIGHTS:

- Igneous and meta-igneous crustal xenoliths in volcanic rocks
- Highly calcic plagioclase (An≥95) produced by partial melting of mafic crust
- Crustal evolution in young volcanic arcs
- Re-working of pre-existing crust induced by emplacement of H_2O-rich picrite magmas

INTRODUCTION

It is widly recognised that arc magmatism plays an importan role in formation and evolution of continetal crust (e.g Taylor and McLennan, 1995). The process of the arc crust formation is driven primary by the addition of mantle derived basaltic magmas. However, arc crust construction and long term evolution involves melt differentiation, crustal melting, melt instruction and possibly cumulate delamination. In principle all of these processes are evident in exume crustal sections of fossil arcs (e.g. Jagoutz and Kelemen, 2015), but they are nutoriously difficult to deconvolve. The currently active arcs can be an anser, a window to crust building processes provided that samples of naicent arc crust, such as t crustal xenolith are available. The latter is abbundnat in the active Lesser Antilles oceacinc arc (e.g. Arculus and Wills, 1980, Mellekhova et al. 2019), which is the focuse of theis study.

The Lesser Antilles intraoceanic island arc (Figure 1a) is renowned for its chemical diversity of lavas and abundance of plutonic xenoliths (e.g. Arculus and Wills, 1980,

Macdonald et al. 2000, Whight et al 2017). These two features provide complementary insights into the evolution of arc crust: erupted lavas represent the end products of differentiation of primary, mantle-derived melts over considerable time and depth, whereas crustal xenoliths provide snapshots of different stages of magma evolution (e.g. Debari *et al.*, 1987, Kay and Kay, 1985, Spiess *et al.*, 2017, Yamamoto *et al.*, 2013, Smith, 2014; Melekhova *et al.*, 2019). Crustal structure can be highly variable due to lateral variations in mechanisms of melt generation and differentiation driven by differences in the delivery of magmatic water along the arc, the architecture of subducted and overriding plates, and the composition and thermal structure of the mantle wedge. These features are all evident in the Lesser Antilles arc (e.g. Cooper et al., 2020, Schlaphorst *et al.*, 2021, Braszus et al., 2021). Similarities in the trace element signature of island arc lavas and bulk continental crust suggest that continental crust formed by processes similar to those taking place in island arcs today (e.g. Barth *et al.*, 2000, Jagoutz and Kelemen, 2015, Plank and Langmuir, 1998). Thus, insights into arc crust construction have implications for crust formation more generally.

The recent shift from traditional concepts of melt-dominated crustal magma chambers to vertically-extensive, mush-dominated architectures (e.g. Hildreth and Moorbath 1988, Bergantz 1995, Cashman *et al.*, 2017) offers a new framework for understanding crust-building processes. An important aspect of these mushy systems is that they grow over hundreds of thousands to millions of years through incremental additions (as sills or dykes) of mantle-derived basalt to form a 'hot zone' in the mid- to deep crust (Annen *et al.*, 2006). Thus, as arc crust grows, new inputs of hot basalt encounter and react with earlier, cooler crustal rocks. Such rocks may represent old, pre-existing crustal lithologies, or ancestral magmas of the same arc-building episode. Evolved hot zone magmas can be produced both by crystallisation of input basalts and (re)melting of crustal rocks (e.g. Jackson et al 2018, Annen et al., 2006).

Crustal architecture and crust-building magmatic processes can be deduced from studies of exposed cross sections of accreted arcs (e.g. Burg *et al.*, 1998, DeBari and Greene, 2011, Jagoutz, 2014, Otamendi *et al.*, 2012). Exhumed, fossil arcs have the advantage over active arcs of containing exposed sections of plutonic rocks from a wide range of crustal depths extending all the way down to the crust-mantle boundary. Conversely, it is not always straightforward to unravel the effect that post-magmatic and post-collisional processes have had on resulting crustal structure and composition. An alternative, complementary approach is to study the petrology and chemistry of active island arcs in combination with geophysical surveys of arc structure (e.g. Allen *et al.*, 2019, Kodaira *et al.*, 2007, Schlaphorst *et al.*, 2018, Shillington *et al.*, 2013). Here we present a detailed petrographic, mineralogical, textural and geochemical study of a diverse collection of crustal xenoliths from Petit St Vincent, Grenadines, Lesser Antilles (Figure 1). Our study of deformed and metamorphosed xenoliths displaying a wide range of different microstructures and pristine igneous-textured xenoliths has enabled us to establish the nature of post- and syn-magmatic crustal processes influencing that are otherwise undetectable at the surface. We analyse the small-scale structures and chemical changes that developed in response to deformation and fluid/melt interaction and make comparisons to unmodified igneous rocks to explore the complexities of arc magmatic processes at depth. Combining our observations with thermal and geochemical modelling allows us to identify processes that led to crust formation under Petit St. Vincent and, by extrapolation, elsewhere in the Lesser Antilles.

GEOLOGICAL SETTING

The active Lesser Antilles volcanic arc, stretching from Saba in the North to Grenada in the South, is the surface expression of westwards subduction of the North and South American Plates beneath the Caribbean Plate (Figure1a). Low subduction rates (~2 cm/yr) have resulted

in limited magma production, with many volcanic islands being small in size and having low eruption frequencies (Macdonald *et al.*, 2000). A recent tectonic model for the evolution of the Eastern Caribbean (Allen *et al.*, 2019, Braszus et al 2021) has highlighted the importance of multi-directional arc migration, outlining three separate subduction systems active at different times: (i) Great Arc of the Caribbean (GAC) whose clearest expression is the submarine Aves ridge (Cretaceous-Paleocene) west of the modern arc, (ii) Outer Arc whose remaining surface manifestation is the Limestone Caribbees (Paleocene-Eocene) and (iii) Lesser Antilles Arc (Miocene to present). Allen *et al.* (2019) propose that the latest arc migration, to form the present-day Lesser Antilles, would have encroached on a pre-existing back-arc basin behind the now extinct Outer Arc. The oceanic crust and sediments of this spreading domain form the original basement on which the volcanic islands of the southern Lesser Antilles were built. North of Martinique, greater crustal thicknesses rule out significant back-arc spreading and imply the development of those islands on older arc crust of the overriding plate (presumably thickened by magmatism of the GAC). This model highlights a clear distinction between the basement of northern and southern Lesser Antilles islands, which may account for along-arc differences in chemical and isotopic signatures of erupted magmas (e.g. Macdonald *et al.*, 2000).

Islands of the southern Grenadines archipelago are among the smallest in size of the entire arc and demonstrate little active tectonism or volcanism (Figure 1). This is in contrast to adjacent larger islands St. Vincent (to the North) and Grenada (to the South), and the active submarine volcano Kick-‘em-Jenny near Grenada, which together emphasise the ‘volcanic gap’ represented by the Grenadines (Bouysse and Westercamp, 1990). Petit St. Vincent is one such Grenadines island, located 64 km south of St. Vincent (Figure 1b). Private ownership of the island has limited previous attempts at sample collection and geological mapping; consequently Petit St. Vincent has been little studied. As with other

subaerial islands of the Grenadines, Petit St. Vincent is no longer considered to be active, with volcanism having taken place almost exclusively in the middle Miocene (Bouysse *et al.*, 1990). Petit St. Vincent lies close to Petite Martinique (Figure 1b) and the islets of Petite Dominique, Fota and Umbrella. The ring-shaped archipelago likely marks out the summit region of a much larger, submerged volcanic edifice.

ANALYTICAL METHODS

Initial petrographic analyses were carried out on thin sections of 19 coarse-grained xenoliths, one dolerite and one basaltic lava collected during a 2011 field campaign. Fourteen representative xenoliths were chosen for further analysis based on textures and mineral assemblages (Table 1). Modal abundances of the major mineral phases were obtained by point counting (1100 to 3000 points per sample) using a mechanical stage. Volume modes were used to classify xenoliths following Streckeisen (1976) (Table 1) and then converted to mass modes using mineral densities (Figure 2) (Deer *et al.*, 2013). Where samples were too altered to be point-counted with sufficient accuracy, mineral modes were not determined, and no specific rocks names assigned (Table 1).

Polished, carbon-coated thin sections of representative xenoliths and lavas were imaged using a Hitachi S-3500N scanning electron microscope with backscattered electrons obtained at 20 or 25 kV. Major element concentrations of minerals and 12 glassy clinopyroxene-hosted melt inclusions (MIs), ranging in size from <10 to 50 μm, were subsequently analysed with a Cameca SX100 electron microprobe. Mineral analytical conditions included 20 kV accelerating voltage, 10 nA beam current and 1 μm spot size; MI analyses used 20 kV accelerating voltage, 5 μm-defocused spot, 4 nA beam current to minimize alkali loss during analysis (Humphreys *et al.*, 2006). Both techniques were calibrated using oxide, mineral and metal standards. Full list of primary and secondary

standards provided in Table A1. Ferric iron contents of minerals were estimated using the stoichiometric methods of Droop (1987) for spinel, Lindsley (1983) for clinopyroxene, and Holland and Blundy (1994) for amphibole.

Trace element concentration were analysed by laser ablation ICP-MS at the Open University using a Photon Machines Analyte G2 193 nm excimer laser system, equipped with a HelEx II 2-volume cell coupled to an Agilent 8800 ICP-QQQ and following procedures established in Jenner and O'Neill (2012). Samples were ablated with a repetition rate of 10 Hz and an energy density of 3.63 J/cm^2. Helium carrier gas 0.9 l/min was mixed downstream in a mixing bulb with ~0.77 l/min Ar carrier gas. Depending on the size of the targeted minerals, different spot sizes (85, 50 or 30 μm) were chosen. For each analysis, 30 seconds of gas-blank were measured, followed by a 30 second ablation signal and a 40 second washout period. Analyses were carried out in batches, with two analyses of reference material NIST SRM 612 and two analyses of reference material BCR-2G conducted at the beginning and end of each batch of ~20 unknowns. The direct mass interference from ^{115}Sn on ^{115}In was corrected for following the methods outlined in Jenner and O'Neill (2012). During the first stage of data reduction, NIST SRM 612 was used for external calibration of data and ^{29}Si was used for internal calibration of data. Signals were carefully evaluated and selected in Iolite to avoid inclusions or mixing of signals into other phases with depth (Paton *et al.*, 2011). Typical analytical conditions and uncertainties are reported in Supplementary Table A5.

Five basaltic lava samples were analysed by X-ray fluorescence spectrometry for major and trace elements using a PANalytical Axios XRF spectrometer at University of Leicester (sample PSVL1b) and a Philips PW1480 XRF at Royal Holloway of London (RHUL: samples PSV1 to 4). Rock powders were ignited at 950 ºC at Leicester and 1100˚C at RHUL, yielding the loss on ignition reported. Major elements were analysed on fused glass discs prepared with a Li-bearing flux at RHUL to minimize matrix effects. Trace

elements were determined on pressed powder pellets, using a PVA binder with boric acid backing at RHUL. Matrix corrections for trace elements at RHUL were calculated from majore elements. Typical uncertainties at RHUL are reported at https://www.royalholloway.ac.uk/research-and-teaching/departments-and-schools/earth-sciences/research/research-laboratories/x-ray-fluorescence-laboratory/ for the current PANalytical Axios; uncertainties were similar on the PW1480.

Electron back-scatter diffraction (EBSD) measurements of two samples (PSV10, 11) were carried out at University of Tokyo using a scanning electron microscope equipped with an EBSD system (JEOL JSM-6510LV with Oxford HKL Channel5), at 20 kV accelerating voltage with a load current of 50-90 mA and a working distance of 26 mm. EBSD patterns were collected in low vacuum (10 Pa) mode. A potential problem with EBSD analysis of lower symmetry minerals has recently been highlighted where the scanning direction and the geometry of EBSD detector can lead to unexpected 180° rotations in the derived crystal orientations (Miyake, 2016). We verified the appropriate configuration for the Tokyo SEM-EBSD machine using a (0001) surface of corundum where the crystal orientation was determined from the external morphology of a well-formed crystal. Crystal preferred orientation (CPO) plots were performed using the MTEX open-source software for Matlab (Bachmann *et al.*, 2010). EBSD mapping was used to determine mineral modes for PSV10 and PSV11; these are reported alongside point count modes in Table 1.

RESULT

Petrography

The xenoliths consist of plagioclase, clinopyroxene, orthopyroxene, hornblende, spinel and ilmenite, together with minor iddingsitised olivine, and accessory apatite. The modally dominant phase is plagioclase (Figure 2). Clinopyroxene is ubiquitous, but never the most

abundant phase. One xenolith is plagioclase-free (PSV3), while two xenoliths are hornblende-free (PSV13, PSV16). Oxide minerals (<8%) occur in 95% of samples. Although magnetite is the predominant oxide phase in these xenoliths, ilmenite is the lone oxide in PSV8 and PSV16. Only in PSV6 do magnetite and ilmenite coexist. Xenolith rock types comprise minor hornblendites and gabbros, the latter consisting largely of the pyroxene-hornblende variety (Table 1). Samples have a range of grain sizes from fine (<300 μm) to coarse (>3 mm). Mineral zoning is widespread. The relative crystallisation order of xenoliths, determined from textural observations of included and interstitial phases, is variable (Table 1).

The sole lava analysed in thin section (PSVL1) contains olivine, clinopyroxene and magnesiochromite spinel phenocrysts. Olivine shows partial alteration to iddingsite around grain rims and interiors; other phases are alteration-free.

Unlike xenoliths from other volcanoes of the Lesser Antilles arc (Arculus and Wills, 1980; Melekhova et al, 2019), 30% of Petit St. Vincent xenoliths display striking deformation microstructures effectively recording metamorphic/metasomatic reactions. Igneous textural nomenclature is therefore not universally applicable. For these reasons, xenoliths are divided into two main groups: igneous and meta-igneous.

Igneous xenoliths (spl + plag + cpx + hbl ± ol ± ap)

This group contains the largest proportion (65%) of collected xenolith samples. Xenoliths are medium (≤3 mm) to coarse grained and may contain recrystallized interstitial melt. Igneous textures range from orthocumulate to adcumulate based on the nomenclature of Wager *et al.* (1960) (Table 1). Samples range from ultramafic (hornblendite, Figure 3a) to hornblende- and/or plagioclase-dominated gabbros (Figure 3b, c). Spinel occurs mainly as inclusions (ø <500 μm) and as cumulus grains (ø <2 mm) in PSV19 (Figure 3c). Iddingsite (0.1%) is only

observed in PSV14 as resorbed chadacrysts in poikilitic hornblende. Plagioclase (~44%) when present is subhedral (ø <2.5 mm) with sieve-textured cores. Clinopyroxene (~28%) is generally subhedral (ø <3 mm) and displays oscillatory and sector zoning (Figure 3c). Replacement of clinopyroxene by hornblende is common (Figure 3c and d). Hornblende occurs as oikocrysts, prismatic grains (ø <6.5 mm) and subhedral intergranular grains (ø <5 mm) (Figure 3). Intergranular hornblendes sometimes contain inclusions of spinel, plagioclase and/or clinopyroxene (Figure 3c). In coarser grained samples, hornblende crystallises slightly earlier in the assemblage. Igneous xenoliths can be further subdivided into two groups based on hornblende textures: those with poikilitic hornblende, and those dominated by subhedral hornblende (Table 1). The latter group often shows replacement of clinopyroxene by hornblende (Fig 3d). Melt inclusions (MIs) are common in this group, but found mainly in clinopyroxene.

Meta-igneous xenoliths (spl + plag + cpx ± opx + hbl ± ilm ± ap)

This group displays textures ranging from those showing relict primary magmatic fabrics (Figure 4a) to those that are intensely deformed with associated grain-size reduction and foliation development (Figure 4b-f). Grain sizes range from coarse to fine. Spinel (magnetite) and ilmenite (<0.1%) are present as inclusions (ø <800 μm) and as microcrystalline interstitial minerals, but are typically less abundant than in igneous xenoliths. In non-foliated samples, plagioclase (~42-53%) is subhedral (ø <6 mm) with sieve-textured cores and rims. In foliated samples, there are cases of sheared porphyroclastic plagioclase grains (ø <2 mm) showing internal deformation and recrystallization, occasionally replacing the entire original large grain with small sub-grains (Figure 4c, d, e). Plagioclase-rich domains are typically surrounded by pseudomorphed clinopyroxene, hornblende and orthopyroxene (PSV18) domains. In some instances where plagioclase and clinopyroxene + hornblende domains

meet, a mortar texture of fine crystals is observed (Figure 4c). Undeformed clinopyroxene in PSV16 exhibits euhedral, prismatic grains (47%, ø <7 mm) (Figure 4a) but in other samples clinopyroxene grains generally show significant internal deformation (PSV18, Fig 4e). Orthopyroxene is a minor mineral and present only in PSV18 and PSV10-2. MIs are preserved only in one sample, PSV8 and hosted in clinopyroxene.

Other deformation microstructures include preferred crystal orientation (Figure 4a), intra- and inter-granular microcracks filled with small mineral grains (Figure 4c), deformation twinning in plagioclase and truncating and interpenetrating grain contacts (Figure 4b, d). The degree of foliation development and recrystallization shows a progression from incipient (Figure 4c) through intermediate (Figure 4d) to mylonitised (Figure 4f), the latter showing evidence of internal strain such as micro-boudinage of plagioclase-rich domains, now fully recrystallised. Foliations are characterised by discontinuous layers of plagioclase interspersed with clinopyroxene-hornblende domains wherein hornblende occupies interstices between clinopyroxene grains as well as forming discrete small aligned grains (Figure 4e and f). Post-deformation crystallisation of hornblende is observed in PSV18 (Figure 4e). Trails of oxide-rich layers are observed in PSV10-2.

In PSV6, microcrystalline (ø <200 μm), equigranular and anhedral crystals of plagioclase, clinopyroxene and hornblende are interspersed with larger subhedral grains of plagioclase (ø <3 mm) and hornblende (ø <2.5 mm), without marked foliation (Figure 4d). These distinct 'megacrysts' suggest textural overprinting. Megacrysts contain inclusions of spinel, plagioclase, clinopyroxene and/or hornblende suggesting relatively late crystallisation.

Lava (spl + ol + plag + cpx) and hypabyssal rock (spl+pl+ilm+cpx)

The single basaltic lava (PSVL1b) and single dolerite (PSV13) studied in thin section are shown on Figure 3e and f. Hornblende is conspicuously absent from the phenocryst

assemblage in both basalt and dolerite. Spinel (ø <400 μm) occurs as subhedral microphenocrysts and inclusions.

The basalt contains subhedral/anhedral, partially iddingsitized olivine (ø <2 mm) and subhedral clinopyroxene phenocrysts (ø <1.3 mm). Some crystals show embayed edges and resorbed interiors. Clinopyroxene grains are subhedral with oscillatory zoning and often corroded interiors. Phenocryst aggregates (glomerocrysts, ø <2.5 mm) in basalt occur as both monomineralic (olivine- and clinopyroxene-only) and polymineralic (spinel, olivine and clinopyroxene) clusters. Plagioclase exists as subhedral laths in the groundmass (ø<700 μm), but never as a phenocryst. The groundmass (≤56 % by volume) consists of microlites of phenocrysts. MIs are lacking.

The dolerite displays medium grained, porphyritic texture with euhedral/subhedral clinopyroxene embedded in an irregular mesh of plagioclase grains. Clinopyroxene shows normal and fine oscillatory zoning, and often contains melt inclusions. Some of the plagioclase and clinopyroxene grains are completely resorbed. Spinel and ilmenite coexist.

Major element chemistry

Full mineral analyses for Petit St. Vincent xenoliths and lava are presented in Table 1A. Unpublished data from Butt (2012) for PSV19, PSV10 and PSV17 are also included. For PSV14, the iddingsitized nature of olivine prevented analysis. For spinel and clinopyroxene, Mg# is expressed as $100Mg/(Mg + Fe^{2+})$ and for hornblende, Mg# is expressed as $100Mg/(Mg + Fe^{Total})$. For the most part, compositional clustering corresponds to the above texturally-defined groupings.

Plagioclase

Plagioclase data are presented in Figure 5. Xenolith plagioclases from the igneous group have a generally narrow compositional range (An_{95-85}) except for those in PSV12 where some rim compositions extend to An_{55}. Plagioclase from the meta-igneous group has a very wide compositional range, An_{99-43}. PSV10-2 contains the most calcic plagioclase of any xenolith, An_{99}. Normal zoning is dominant in both xenolith groups. Reverse zoning is rare and insignificant, with rimward increases of only 2 to 4 mol% An (e.g. PSV20 An_{86} to An_{90}). There is no clear correlation between iron concentration and An content in both igneous and meta-igneous xenoliths (Figure 5a). Potassium concentrations decrease with increasing An (Figure 5b).

Plagioclase composition in the meta-igneous group varies with texture. There is a marked compositional change from relict igneous plagioclase to newly re-crystallised parts of the same grain. This is, best seen in sample PSV17 (Figure 4b) where plagioclase An content increase by almost 20%, from An_{77} in relict cores to An_{96} in late-stage plagioclase. Newly formed plagioclase also contains less Fe and K (Figure 5a andb). There are two, texturally distinct generations of plagioclase in PSV6 (early equigranular and late anhedral crystals), however compositionally the two generations are indistinguishable. In PSV10-2 we did not find any original grains; the sample is completely re-crystallised to new, highly calcic compositions (An_{99}) suggesting that the process captured in PSV17 has proceeded to completion in PSV10.

Microlite plagioclase from lava has a narrow range in compositions ($An_{87–82}$) with minimal zoning, in contrast to extensively zoned plagioclase phenocrysts from dolerite (An_{87-52}). Fe concentrations in dolerite (PSV13) increase with decreasing An until An_{73} (Fe 0.036 pfu) after which Fe contents gradually decrease with decreasing An (Figure 5a), probably reflecting the onset of ilmenite or titanomagnetite crystallisation. There is a clear divergence

at ~An_{84} in Fe contents of plagioclase from meta-igneous xenoliths and plagioclase from lava, dolerite and igneous xenoliths (Figure 5a).

Pyroxene

In the igneous xenoliths clinopyroxenes are diopside with a range in Mg# from 92 to 73, while in the meta-igneous xenoliths the range in Mg# is 96 to 65 (Table A1). Normal zoning is prevalent in both xenolith groups, with rimward decreases of up to 16% Mg# (e.g. PSV10-2 Mg#85 to Mg#69). Reverse zoning is rare with rimward increases up to only 3% Mg# (e.g. PSV3 Mg# 89 to92). Oscillatory zoning is a recurrent feature in the igneous xenoliths. Calcium content shows no discernible trend with Mg# (Table A1).

Clinopyroxene phenocrysts from lava and dolerite have Mg# ranges from 98 to 77 and 85 to 75, respectively, and, in common with the igneous xenoliths, the compositions are diopside. Normal zoning is predominant with rimward decreases of <21% (e.g. Mg#98 to Mg#77). Calcium contents do not vary significantly with Mg# (Table A1).

Clinopyroxene of the meta-igneous xenoliths are depleted in Ti and Al^{IV} compared to those of the igneous xenoliths, lavas and dolerite (Figure 6a). There is a divergence in compositional trends of clinopyroxenes at Ti contents of ~ 0.015 (p.f.u. Figure 6a) and two almost parallel trends can be identified: the first is defined by clinopyroxenes from lava, hornblende-free xenoliths and xenoliths with subhedral hornblende; the second comprises clinopyroxenes from dolerite and xenoliths with poikilitic hornblende. Clinopyroxene from dolerite shows a continuous sequence of core to rim variations based on Mg#. The evolution follows a loop and is illustrated by the green arrow on Figure 6a. In Figure 6b, we show Ti vs Al^{IV} for clinopyroxenes from fractional crystallization experiments of Ulmer et al. (2018) and Nandedkar et al. (2014), carried out on a basaltic starting compositions. These experimental studies span an extensive range of magmatic temperatures and therefore represent well the

differentiation sequence of clinopyroxene, which displays similar loops to those observed in the igneous xenoliths (Figure6a). In detail, the shape of the differentiation loop is controlled by the crystallising assemblage. The onset of amphibole crystallization at 1080ºC (blue diamond, (Ulmer *et al.*, 2018) Figure6b) changes the relationship between Ti and Al^{IV}. In the experimental sequence of (Nandedkar *et al.*, 2014) the change is more subtle as a result of plagioclase crystallization following prolonged crystallisation of olivine + clinopyroxene.

Orthopyroxene, only found in meta-igneous xenoliths PSV18 and PSV10-2, has a compositional range of $En_{80–82}$ ($Mg\#_{82–84}$). Tetrahedral aluminium and Ti contents are low (0.04–0.01 pfu and 0.005–0.001 pfu) and negatively correlated with Mg#. There is no correlation between Ca content (0.03–0.05) and Mg# (Table 1A).

Amphibole

Xenolith amphiboles are magnesiohastingsite and edenite according to the classification scheme of Leake *et al.* (1997). Amphibole is restricted to magnesiohastingsite in the igneous xenoliths, whereas in the meta-igneous xenoliths composition are mainly edenite with a few compositions transitional to magnesiohastingsite. We use the collective term hornblende to describe all amphiboles in the studied rocks. Meta-igneous xenolith hornblendes extend to slightly higher Mg# than those from igneous xenoliths; 84 to 62 and 82 to 57 respectively (Figure 7a). Normal and reverse zoning are common in the two xenolith groups with both rimward decreases and increases of <7% (e.g. PSV3 $Mg\#_{70}$ to $Mg\#_{77}$; PSV8 $Mg\#_{68}$ to $Mg\#_{70}$). The meta-igneous group shows a general decrease in Al^{IV} (pfu) with increasing Mg# (Figure 7a). Al^{IV} contents in this group extend to very low concentrations. These features are similar to those described by Blundy and Holland (1990) for amphiboles from Adamello Batholith, Italy, where they were interpreted in terms of oxidation (increasing Mg#) during cooling (decreasing Al^{IV}) rather than simple magmatic differentiation. The igneous group

shows no clear correlation between Mg# and Al^{IV}, and the range of Al^{IV} is higher than the meta-igneous group, but more limited in range suggesting higher (and sustained) crystallization temperature.

Chlorine concentrations in xenolith hornblendes are elevated (≤ 0.33 wt.%), with those from the igneous xenoliths having higher concentrations than those from the meta-igneous xenoliths. Chlorine concentrations increase with K_2O for hornblendes from both groups (Figure 7b). However, the igneous group hornblendes show a much steeper slope for a Cl vs K_2O plot, compared to the meta-igneous group. The lowest concentrations of Cl and K_2O are in strongly deformed meta-igneous xenoliths PSV10 and PSV18.

Spinel

Xenolith spinel compositions are predominantly titaniferous magnetite (Table A1, FigureA1). Dolerite (PSV13) also contains magnetite, but with notably higher Ti contents (Figure A1). In contrast, spinels from Petit St. Vincent lava are Mg- and Cr-rich ($Mg\#_{67–34}$;$Cr\#_{62–41}$; Figure A1). Comparable Cr contents ($Cr\#_{47–42}$) are only observed rarely in igneous xenoliths, notably PSV3 and PSV14. Spinels are relatively rare in meta-igneous xenoliths, so analyses are more limited. Unusually, meta-igneous xenolith PSV6 contains Cr-rich spinel ($Cr\#_{70–38}$) with low Mg# (5-9).

Bulk rock compositions

Five Petit St. Vincent lavas were analysed for whole-rock major and trace elements.
In Figure 8 bulk rock major element data for Petit St. Vincent from this study (Table A2, Supplementary) and whole-rock lava data from other Grenadines volcanoes (Bequia, Kick‘em-Jenny, Kick-‘em-Jack, Canouan and Mustique), Grenada and St. Vincent are shown for comparison. The whole-rock data and petrographic observations show that Petit St.

Vincent lavas are Mg-rich basalts compositionally very similar to picritic lavas from other Grenadines islands, St Vincent and Grenada (Figure 8).

Bulk rock major element compositions of xenoliths were calculated from point-counted mineral mass modes and averaged mineral compositions. Uncertainties on the recalculated whole-rock compositions in Figure 8 were fully propagated from standard deviations of mineral compositions and point count modes. Bulk rock compositions for PSV10 and PSV18 could not be determined because samples were too altered to be point counted accurately. Our inability to measure the major element composition of iddingsitised olivine for PSV14 also prevented bulk rock calculations. The meta-igneous xenoliths are lower in FeO, in keeping with their low Fe-Ti oxide contents, and higher in SiO_2 than the igneous xenoliths.

Xenolith melt inclusions

Melt inclusions in clinopyroxene were found in dolerite (PSV13) and both xenolith groups. Melt inclusions are clear to pale brown in transmitted light and vary in shape from rounded to irregular. They often have gas bubbles, which may contain substantial concentrations of CO_2. Melt inclusions have low $Kd_{Fe\text{-}Mg}$ values with their clinopyroxene hosts compared to experimental *Kd* values. This suggests that melt inclusions have undergone some post-entrapment crystallisation. Corrections for post-entrapment crystallisation (addition of host mineral back to melt inclusion until equilibrium reached), made using an experimental *Kd* value of 0.28 (Melekhova et al. 2017), range from 1 to 11%. Corrected and uncorrected melt inclusion compositions are reported in Table A3.

Melt inclusions EPMA totals are ≥91 wt.%, implying a substantial fraction of dissolved volatiles. Corrected melt inclusions compositions normalised to 100% anhydrous vary from 61.9 to 69.4 wt.% SiO_2 and 0.6 to 2.3 wt.% MgO (Figure 8a). Overall, melt

inclusions describe a fractionation trend from andesite to dacite (Figure 8). Such compositions are more evolved than xenolith whole-rock compositions, but resemble dacite and trachyandesite from the adjacent island of Petite Martinique (Rojas-Agramonte *et al.*, 2017, Figure8). The most evolved melt inclusions (>68.1 wt.% SiO_2) were found in the meta-igneous xenolith group. Melt inclusions from dolerite (PSV13) are high both in K_2O and Na_2O, 4.4 – 5.4 and 5.0 – 7.2 wt.% respectively (Figure 8e and f).

Chlorine contents in Petit St. Vincent melt inclusions are remarkably high: 0.4 to 0.9 wt.%, especially when compared to melt inclusions from Bequia and St. Kitts, ≤ 0.4 and 0.3 wt% respectively. Melt inclusions from igneous xenoliths and dolerite contain, on average, higher Cl concentrations than from meta-igneous xenoliths, albeit we have melt inclusions from only one sample (PSV8). Sulphur contents are high, ranging from 260 to 3900 ppm.

Intensive parameters

Knowledge of magma storage conditions in terms of T–P–H_2O–fO_2 for xenoliths and lavas is important for understanding the magmatic system beneath Petit St. Vincent. A combination of geothermooxybarometers was applied to xenoliths (Table 2): magnetite-ilmenite (Andersen and Lindsley, 1985, Ghiorso and Evans, 2008), hornblende-plagioclase (Holland and Blundy, 1994) and clinopyroxene-orthopyroxene (Putirka, 2008, Wells, 1977). Temperature and fO_2 estimates for co-existing oxides were made using the ILMAT program of LePage (2003) with the Lindsley and Spencer (1982) method for recalculation. The most calcic plagioclase that can be used in the hornblende-plagioclase thermometer is An_{90}. Although some xenolith plagioclases contain higher anorthite contents, only temperatures calculated using An<90 are reported. Post entrapment crystallisation (PEC) effects prevent the use of mineral-melt thermometers. The olivine-spinel oxybarometer of Ballhaus *et al.* (1991) was applied to the lava (Table 2). Major element data for touching rims and/or

included phases and their hosts were used in most hornblende-plagioclase and all olivine-spinel calculations to ensure textural equilibrium in zoned phases. For hornblende-plagioclase in PSV18 and all samples containing clinopyroxene-orthopyroxene and spinel-ilmenite, grains were never contiguous, therefore in these cases, all combinations of grain pairs in each sample were used for calculations and the results averaged. A nominal value of 500 MPa was used where a pressure estimate was needed for temperature calculations. This was deemed acceptable based on crustal reconstruction under the southern part of Lesser Antilles (Melekhova *et al.*, 2019).

We were only able to calculate pressures for one xenolith (PSV18) using cpx-opx barometery (Putirka, 2008). The pressure range for this meta-igneous sample is 397 – 457 MPa (Table 2).

There is good agreement (±61 °C) between different thermometers applied to the same samples. Xenolith temperatures range 790–1039 °C, while the lava records higher temperatures of 1014–1095 °C. The broad temperature range of xenoliths is consistent with the diversity in textural groups suggesting contrasting formation histories. For the most part, there is a general decline in temperatures from the igneous to the meta-igneous group, although all estimated temperatures are supra-solidus suggesting the presence of melt during deformation. Oxygen fugacity (*f*O2) estimated for xenoliths ranges from 0.5 to 1.8 log units above the NNO buffer. For the lava, fO_2 ranges from 2.7–2.9 above NNO, suggesting that it is more oxidised than the xenoliths.

Trace element chemistry

Selected trace element data for minerals and rocks are plotted in Figures 9 to 12. Data are plotted either as mass fraction concentrations (ppm) or as primitive upper mantle-normalised REE concentrations (Figure 10) using values of Palme and O'Neill (2003). For more detailed

descriptions of the geochemistry of lavas from Grenada and the Grenadines the reader is referred to White *et al.* (2017). In this context, Petit St. Vincent lavas (Table A2) display trace element patterns that are very similar to M-series picrites from Grenada. To illustrate the mineral trace element data from Petit St. Vincent we have chosen elements that best illustrate key characteristics and evolutionary trends, noting where appropriate other elements that show similar behaviour. Strontium is used for the abscissa on all mineral plots, as this element best brings out the differences between xenolith types and lavas.

Plagioclase

Plagioclases are enriched in LREE with well-developed Eu anomalies (not shown). Strontium contents are highly variable, from ≤1000 ppm in meta-igneous xenoliths to >1000 ppm in igneous xenoliths, however within each xenolith group there is considerable variation (Figure 9). Lava plagioclases have intermediate Sr contents around 800 ppm, zoning from higher values in the cores to lower in the rims. The highest Sr contents are found in plagioclases from igneous xenolith PSV20, which reach extreme values of ~2500 ppm, indicative of crystallisation from Sr-rich melts, similar to the C-series, 'ankaramitic' lavas of Grenada (Thirlwall et al, 1996; White et al. 2017). The La (and other LREE) content of these plagioclases is consistently low (1-3 ppm La), in contrast to all other igneous xenolith plagioclase that have lower Sr, that extend along an orthogonal trend to >7 ppm La (Figure 9a). Core to rim zoning in plagioclase from PSV12 records a more than two-fold increase in La. This evolution is reminiscent of the evolution of M-series, 'picritic' lavas from Grenada (Figure 9a inset – Thirlwall et al., 1996; White et al. 2017). Broadly similar behaviour is evident in Ba, although the Ba enrichment of the igneous xenoliths relative to PSV20 and intra crystal zoning are less pronounced (Figure 9b). This is consistent with the observation that C- and M-series lavas have proportionately less divergent Ba contents (Figure 9b inset –

Thirlwall et al., 1996; White et al. 2017). The two igneous xenolith plagioclase trends share a common origin with the Petit St. Vincent lava plagioclases for Sr, LREE and Ba, as noted also for whole-rock data (Figure 9a,b inset). Rubidium (not shown) shows similar behaviour to Ba. In terms of the trace elements Li (Figure 9c) and Cu (Figure 9d), there is no discernible difference between PSV20 and the other igneous xenoliths. Li contents for all igneous xenoliths cluster around 2 ppm (Figure 9c – no Li data are available for the lavas). Cu contents are highly variable in the igneous xenoliths and in the lava, reaching >80 ppm is one plagioclase grain from lava. Lead contents of igneous xenolith plagioclases (not shown) are uniformly at or below detection limits, whereas lava phenocrysts have 30 to 45 ppm Pb.

The meta-igneous xenoliths also form two discrete groupings. Three of the xenoliths (PSV6, PSV10, PSV18) have low Sr and La (Figure 9a), but highly variable Ba and Li, extending to concentrations well in excess of any igneous xenolith plagioclases (Figure 9b, c). In contrast, plagioclases from meta-igneous xenolith PSV8 are very similar to the low-Sr group of igneous xenoliths. This is consistent with PSV8, a granoblastic pyroxene-hornblende gabbro, showing relatively few textural indications of metamorphism other than recrystallization (Figure 4c). Cu contents of the meta-igneous xenoliths are highly variable, with an overall range comparable to the igneous xenolith plagioclases (Figure 9d).

In summary, plagioclases in igneous xenoliths appear to reflect crystallisation from distinct magma batches beneath Petit St. Vincent, similar to the C- and M-series lavas of Grenada. Metamorphism, as evidenced texturally, appears to have depleted plagioclases in Sr and enriched them in Ba and Li in a manner that is not observed in lavas from Grenada. An exception is meta-igneous xenolith PSV8 whose plagioclases seem to more closely preserve an igneous geochemistry despite textural evidence of recrystallization.

Clinopyroxene

In terms of REE there is a clear difference between clinopyroxenes from igneous and meta-igneous groups (Figure 10a, b). Clinopyroxenes from igneous xenoliths and lava (PSVL1b) show similar, convex-up REE patterns with slight enrichments in MREE (Nd-Sm) compared to LREE and HREE and modest to absent negative Eu anomalies (Figure 10a). The spread in REE contents of xenolith clinopyroxenes exceeds that of the lavas, which show general enrichment in phenocryst rims relative to cores. The most REE-depleted xenolith clinopyroxenes, which overlap lava clinopyroxenes almost precisely, are found in PSV3. This is the most primitive xenolith in terms of its mineral chemistry (e.g. clinopyroxene Mg#) and plagioclase-free pyroxene hornblendite assemblage (Figure 3a and Table 1). REE patterns of PSV20 and other igneous xenoliths are very similar, consistent with the broad similarity of REE patterns in C- and M-series lavas observed by White et al. (2017)

Clinopyroxenes from the meta-igneous group show a much larger range in REE concentration than the igneous xenoliths and lavas. As for plagioclases, there are two groupings of meta-igneous xenoliths. PSV6, PSV10 and PSV18 are notably depleted in all REE, with relatively spiky patterns due to low concentrations (below PUM) for most REE. Both negative and positive Eu anomalies are observed. A single clinopyroxene from PSV6 is enriched in La. Such depleted REE patterns do not resemble those expect for precipitation from any reasonable melt composition, suggesting significant chemical modification during metamorphism. The exception is clinopyroxenes from PSV8 that show a distinctive REE pattern with enrichments in LREE relative to MREE and HREE. Although more consistent with crystallisation from melt, this pattern is nonetheless distinct from igneous xenoliths (Figure 10a), despite similarities between PSV8 plagioclases and those of igneous xenoliths (Figure 9).

In terms of individual trace elements (Figure 11) broadly similar features emerge to those shown by plagioclases (Figure 9), although with some key differences. PSV20

clinopyroxenes are again enriched in Sr relative to other igneous xenoliths, but show much less variability in the incompatible lithophile elements La (Figure 11a), Zr (Figure 11c) and Ta (Figure 11d) which vary by factors of ~9, ~16 and ~30 respectively, across the igneous group. Hafnium and Nb behave similarly to Zr and Ta respectively. For individual samples variation in these trace elements correlates approximately with Al_2O_3 content of the clinopyroxenes, which is higher in rims than in cores, as indicated for selected samples in Figure 11a,c. Clinopyroxene aluminium content is known to increase the clinopyroxene-melt partition coefficients for high-charge cations, with the greatest effect for the more highly charged cations (e.g. Wood and Blundy, 2001), consistent with the data in Figure 11 for La^{3+} to Zr^{4+} to Ta^{5+}. Consequently, some of this trace element variability in clinopyroxene is a result of changing partitioning behaviour, rather than simply an increase in melt trace element concentration. Petit St. Vincent lava clinopyroxenes show a comparable (or greater) wide range in La, Zr and Ta content to the igneous xenoliths that again correlates with Al_2O_3 content. For Li (Figure 11b) variability is more muted, consistent with its lower charge, and greater in the Petit St. Vincent lava clinopyroxenes than in any of the igneous group xenoliths. The most primitive igneous xenolith, PSV3, is characterised by very low contents of all trace elements.

Meta-igneous clinopyroxenes are consistently displaced to lower Sr, including those from PSV8, which no longer resemble igneous clinopyroxenes as was the case for plagioclases (Figure 9). The considerable variability in La (Figure 11a) and Zr (Figure 11c) in PSV8 clinopyroxenes is correlated with Al_2O_3 content. Notably, the range in Li contents of meta-igneous clinopyroxenes (Figure 11b) is much greater than for all other clinopyroxenes, with the highest concentrations in intensely deformed PSV10 (Figure 11b). Clinopyroxenes from this xenolith are also highly enriched in Cu, Pb Sn and In (not shown). Extended, PUM-

normalised trace element patterns for all Petit St. Vincent xenolith clinopyroxenes are presented in Supplementary Figure A2.

Amphibole

Amphiboles from igneous xenoliths show strikingly similar patterns to clinopyroxene but with slightly higher overall REE contents and almost no Eu anomaly (Figure 10c). Due to the small size of amphibole rims only single rim analysis was possible (from PSV3), which shows slight depletion in LREE compared to cores. MREE and HREE concentration in amphibole from PSV20 are slightly lower compared to the rest of the igneous group. Petit St. Vincent lava does not contain any amphiboles for comparison. Amphiboles from meta-igneous xenoliths show considerable variability with both LREE-depleted and –enriched patterns and Eu anomalies. These patterns are hard to reconcile with any simple process of igneous differentiation.

In terms of selected trace elements (Figure 12), igneous amphiboles are enriched in Sr compared to meta-igneous amphiboles, with the highest concentrations again seen in PSV20. The spread in Zr (Figure 12a) and La (Figure 12b) contents of the igneous group is less than that of clinopyroxenes (Figure 11a, c). This is consistent with less variable partition coefficients for these elements into amphiboles, which are controlled by Ca partitioning between amphibole and melt (Nandedkar et al., 2016) rather than Al_2O_3 content. Thus the observed variability likely reflects variability in melt CaO content, rather than strong crystal-chemical effects on partitioning, as seen for clinopyroxene. The extended trace element patterns for amphiboles from igneous xenoliths (Supplementary Figure A3) show broadly coherent patterns for all elements except for Cr, Th and U. Cr is a highly compatible element during Cr-spinel fractionation, whereas U and Th are highly incompatible. Thus, although the dispersion in Cr contents may be ascribed to crystallisation, this is not a plausible explanation

for the variability in U and Th, which extends over almost two orders of magnitude for igneous xenoliths. Furthermore, there is a marked change in Th/U with decreasing Th from Th/U > 1 at high Th, to Th/U <1 at low Th. There is also a change in the relative fractionation of Sr from adjacent LREE (Pr, Nd), with the development of both negative and positive Sr anomalies, the latter most pronounced in PSV20. These distinctive incompatible trace element behaviours will be discussed in the context of magma differentiation processes in a later section. Again, amphiboles from primitive igneous xenolith PSV3 have the lowest concentrations of all trace elements.

Meta-igneous amphiboles show great variability (up to a factor of 100) in Zr, La, Li and Ba at low, but variable, Sr content. PSV8 again has lithophile trace element contents (Ba, La, Zr) that resemble igneous grains, but with lower Sr (Figure 12). In contrast to plagioclase, meta-igneous amphiboles show a very limited range of Ba contents (Figure 12d); Rb (not shown) shows similar behaviour. Lithium (Figure 12c) contents are significantly higher than in the igneous group. The extended trace element patterns of meta-igneous amphiboles (Supplementary Figure A3) display at least one order of magnitude variability in all incompatible elements as well as Cr. The latter variability is comparable to that of the igneous xenolith amphiboles. In general, the extent of variability increases with increasing incompatibility, from Sc to Th. U and Th show extreme depletion, but unlike the igneous amphiboles Th/U is consistently >1 even in the most depleted grains. Likewise, Sr is always depleted relative to adjacent REE, Pr and Nd. Rb/Ba ratios change from <1 to >1 with increasing depletion. Rb and Ba contents are both higher and lower than in igneous amphiboles (Figure 12d).

In both igneous and meta-igneous amphiboles there is considerable variability in Li (Figure 12c), Cu, Zn and Pb (Table A4). The correlated behaviour of these elements, despite their different incorporation into silicate and sulphide minerals suggests the presence of small

amounts of saline fluid inclusions (brines) in the analysed volume because all of these trace elements are known to complex strongly with chloride ligands (Kouzmanov *et al.*, 2012). As far as possible these brine inclusions have been filtered from the time-averaged LA-ICP-MS signal. However, the likely presence of brines at these conditions is noteworthy.

Electron back-scattering diffraction (EBSD) results

To better understand the trace element chemistry from minerals in the igneous and meta-igneous xenoliths in the context of their microstructural characteristics we performed EBSD analyses on two representative samples: pyroxenite hornblende gabbro (PSV11, Fig. 3d) and mylonitic amphibolite (PSV10, Fig. 4f). These two samples correspond to end members of the xenolith microstructural range we present here. Results are plotted as crystal preferred orientation (CPO) patterns, alongside photomicrographs, in Figure 13.

PSV11 shows a well-developed igneous fabric consistent with crystal precipitation from melt and subsequent settling. Plagioclase grains show a clear flow foliation under the optical microscope (Fig, 13a,b). The plagioclase CPO is typical for magmatic fabrics with a concentration of the (010) poles, normal to the twin planes (Fig. 13a), oriented perpendicular to the foliation and the poles to (100) and (001) forming girdles parallel to the foliation (Fig. 14a) (Satsukawa et al 2014). Clinopyroxene shows a similar, albeit less intense, flow-related alignment. In contrast, the amphibole CPO is somewhat weaker with a less well-developed girdle. The amphibole commonly has cores of clinopyroxene and well-formed crystal faces. These features suggest the CPO of the amphibole is controlled by the original orientations of the clinopyroxene grains either through topotactic replacement or epitactic overgrowth under static conditions rather than directly reflecting magmatic flow. This interpretation is consistent with petrographic observations (Fig. 3d and 13b).

PSV10 shows a quite different microstructure from PSV11 with pervasive grain size reduction of the original plagioclase and clinopyroxene associated with development of a clear foliation. The local presence of relict clasts of both plagioclase and clinopyroxene with strong undulose extinction and well-developed subgrains suggests that grain size reduction was due to dislocation formation and migration (Fig. 13d). Despite this evidence for strong plastic deformation the CPO patterns for the plagioclase and clinopyroxene of PSV11 are almost random (Fig. 13f). The development of strong CPO patterns is a characteristic of deformation accommodated by dislocation creep and their absence in this strongly deformed sample implies different deformation mechanisms were active. Grain boundary sliding suppresses the development of CPO patterns and can largely obliterate former CPO patterns in a rock (Wallis et al. 2011). Grain boundary sliding needs to occur in tandem with an accompanying mechanism able to fill the gaps that open due to the misfit of grains as they slide past one another. Suitable mechanisms are solid state diffusion or solution and precipitation facilitated by flow of a fluid or melt. Detailed observations of the strongly deformed domains (Fig. 13e) show they dominantly consist of bimodal mixtures of either plagioclase with smaller grains of clinopyroxene, or clinopyroxene with similar-sized grains of amphibole. Some of the small amphibole grains are aligned, whereas others appear to fill in pore-space around clinopyroxene grains. This behaviour is reflected in the amphibole CPO (Fig. 13f), which shows a concentration of (001) poles and weak girdle development normal to (100) and (010). In contrast to PSV11, the amphibole CPO does not mimic that of clinopyroxene. These features of the amphiboles CPO can be explained as the result of oriented growth within dilational space opened up as grains slid past one another possibly accentuated by mechanical rotation of needle shaped grains. The long axis of the amphibole corresponds closely to the concentration of (001) poles and indicates the direction of maximum extension.

Mechanical mixing of grains during grain boundary sliding is possible but the fine-scale mixing of plagioclase and clinopyroxene grains is present even in relatively weakly deformed domains. If plagioclase-clinopyroxene mixing was due solely to mechanical processes then high strain domains should be more greatly mixed than others. This is not observed. The weak CPO patterns for plagioclase and amphibole in PSV10 support the idea that deformation subsequent to subgrain formation was accommodated by sliding along the new grain boundaries (Fig. 14b). A striking feature of the plagioclase-rich domains is the presence of tiny voids at grain triple-junctions (Fig. 13e), suggestive of the original presence of fluids during recrystallization. Fluid infiltration may have been promoted by the formation of gaps between the grains as they slid past one another.

DISCUSSION AND INTREPRETAION

Textural Evidence for Fluid-fluxed melting

The above microstructural observations including crystallographic and shape preferred orientation types suggest that deformation took place in the presence of an intergranular fluid or melt resulting in the crystallization of secondary phases in dilational sites between recrystallized grains in both pyroxene- and plagioclase-rich domains.

In addition to demonstrably magmatic primocrysts of amphibole, such as those in igneous xenoliths PSV3 (Figure 3a) and PSV20 (Figure 3b) there is strong petrographic evidence of later formation of amphibole at the expense of clinopyroxene, plagioclase and oxides in both igneous (Figure 3c,d) and meta-igneous xenoliths (Figure 4a-f). Amphibole formation is likely to have occurred via incongruent, melt-forming reactions of the type: $cpx_1 + pl_1 + ox_1 + fluid = amph \pm pl_2 \pm cpx_2 + ox_2 + melt$. The reactant hydrous fluid could derive internally, due to enrichment during crystallisation, or externally through addition of fluids from another magmatic source. That source could also provide heat. Regardless of the fluid

source, progressive development of the above reaction could generate poikilitic amphibole (Figure 3c) or amphibole pseudomorphs after clinopyroxene (Figure 3d), consistent with inheritance of clinopyroxene CPO fabrics by amphibole (Figure 13c). These textures can be envisaged forming at supra-solidus magmatic conditions, producing amphiboles with magmatic chemical signatures (Figure 10c) that resemble those of precursor magmatic clinopyroxene in terms of REE (Figure 10a). However, other chemical features of the igneous amphiboles, such as their U-Th systematics noted above, suggest a more complex origin than simple, closed system magmatic crystallisation. This will be explored in more detail below.

In contrast, meta-igneous xenoliths PSV8, PSV18, PSV6 and PSV10 have clinopyroxene (Figure 10b) and/or amphibole (Figure 10d) trace element characteristics quite unlike igneous xenoliths (or Petit St Vincent lavas). These xenoliths are extensively re-equilibrated, but are undoubtedly metamorphic rocks with original igneous protoliths. The depleted nature of the incompatible elements in meta-igneous amphiboles (e.g. Th, U, La, Nb, Ta) is suggestive of some partial melting accompanying metamorphism, and is consistent with our EBSD analyses that imply the presence of an intragranular fluid or melt phase (Figure 13e,f) during deformation. Melting may have been triggered by the addition of aqueous fluids that passed along grain boundaries or fractures developed during deformation. The influx of such a fluid is evidenced by elevated Li contents in meta-igneous amphibole and clinopyroxene compared to igneous xenoliths (Figure 11 and 12). The wide variety of trace element patterns within individual amphiboles from single samples is indicative of poor diffusive re-equilibration. It is significant that amphibole grains in PSV10 display both positive and negative anomalies for Pb and Li (Supplementary Figure A3) and these are associated with clinopyroxene grains that show a large scatter in the concentrations of the same elements (Supplementary Figure A2). All these reaction textures and Al-poor nature of the meta-igneous amphiboles (Figure 7a) indicate lower temperatures than those of the

igneous xenoliths, mineral thermometry (Table 2) indicates supra-solidus conditions (≥790 °C). We envisage amphibole formation in a dynamic environment (high temperature shearing in a crystal mush state) for formation of these meta-igneous xenoliths.

Some meta-igneous xenoliths (e.g. PSV8) have mineral trace element and recalculated major element compositions that resemble the igneous xenoliths. Other meta-igneous xenoliths, notably PSV10, are chemically quite distinct and may represent pre-magmatic basement crust, rather than precipitates from any particular erupted magma. If this is correct these samples may be significantly older than the present day magmas erupted on Petit St. Vincent. Geochronology would help test this idea; but such ages are not available and no zircon was observed in the studied samples in thin section or in mineral separates. As the original magmatic composition of these rocks is likely to have been modified by metamorphic processes, it is not possible to deduce their original compositions from mineral trace element chemistry alone, other than to infer a broadly mafic, igneous protolith.

Origin and evolution of igneous xenoliths

The trace element patterns of minerals from the igneous xenoliths are sufficiently coherent to be used to explore both the magmatic origin of the constituent minerals and the igneous processes that shaped their chemical evolution. Possible processes include closed system fractional and equilibrium crystallisation, and fractional and equilibrium partial melting, as well as open system crustal assimilation and melt percolation, and diffusion, all of which may have operated during the history of the igneous xenolith suite.

To interpret mineral trace element compositions in terms of magmatic processes requires knowledge of mineral-melt partition coefficients for as wide a range of analysed trace elements as possible. Because partition coefficients (Ds) vary as functions of mineral and melt chemistry and the prevailing intensive variables (P-T-fO$_2$) during crystallisation, it

is important to use a consistent set of Ds rather than simply mix and match Ds from different systems obtained under different conditions. For this reason, we focus on amphibole for which the experimentally-determined Ds values of Nandedkar et al. (2016) provide an internally consistent parameterisation for 27 of the trace elements analysed in our study, over a range of temperatures (1010 to 730 °C) at 0.7 GPa pressure, conditions broadly consistent with those of the igneous xenoliths.

For each trace element, *i*, Nandedkar et al. (2016) parameterise the partition coefficient (D_i) as a function of the Ca partition coefficient (D_{Ca}):

$$ln(D_i) = A_i ln(D_{Ca}) + B_i \quad (1)$$

where A_i and B_i are constants derived by multiple regression of the experimental data specific to each trace element. For all trace elements studied here, except K, Rb and Ti, these values (and their uncertainties) are those provided in Table 7 of Nandedkar et al. (2016). For Ti we simply fitted the same experimental dataset of Nandedkar et al. (2016), to obtain the fit parameters: A_{Ti} =1.11±0.11 B_{Ti} = 0.507±0.095. For Rb, we assumed a constant D_{Rb} (0.090), as only two experiments were analysed for this element.

Parameterisation in terms of D_{Ca} is advantageous because the CaO content of amphibole is relatively constant (~11.5 ± 0.5 wt%) and the CaO content of potential parent magmas, as recorded by lavas (Figure 8), is known. To reduce the number of parameters that can be independently varied, we have further parameterised D_{Ca} as a reciprocal function of temperature, *T*, using the Nandedkar et al. (2016) experimental data (T in Kelvin):

$$D_{Ca} = \exp\left(\frac{6662 \pm 366}{T} - 4.83 \pm 0.33\right) \quad (2a)$$

The partition coefficient for K was also fitted to reciprocal temperature rather than D_{Ca}, as this provides a better parameterisation of the Nandedkar et al. (2016) data:

$$D_{\mathrm{K}} = \exp\left(6.15 \pm 0.49 - \frac{8985 \pm 606}{T}\right) \quad (2b)$$

The calculated *D*s values for the 26 trace elements, along with their uncertainties propagated from fitting errors on A_i and B_i are presented in Supllmementary Figure A5 for a representative D_{Ca} = 1.7 (970 °C). Note that all *D*s are of similar precision (±30% relative) except for U (80%), Th (90%) and Pb (~100%). The very large errors on *D*s for the last three elements means that the calculated melt compositions should be treated with caution, likely because factors other than D_{Ca} alone influence their partition coefficients.

To improve the uncertainty on the calculated values of D_U and D_{Th} we have explored alternative parameterisation approaches to the Nandedkar et al. (2016) data. We find that weighted regression D_{Th} and the ratio D_{Th}/D_U against reciprocal temperature (*T* in Kelvin) yields an improved fit, as follows (1 s.d. uncertainty):

$$D_{\mathrm{Th}} = \exp\left(\frac{18973 \pm 2348}{T} - 19.35 \pm 2.00\right) \quad (3a)$$

$$D_{\mathrm{Th}}/D_{\mathrm{U}} = \exp\left(\frac{-3199 \pm 919}{T} - 2.91 \pm 0.77\right) \quad (3b)$$

These expressions lead to an increase in D_{Th} with decreasing temperature, and a cross over from D_{Th}/D_U >1 to <1 at 810 °C, in accord with the experimental data of Nandedkar et al. (2016).

Parent melt for igneous xenoliths

As a first step we used equation (1) to explore the trace element pattern of possible parent melts for igneous xenolith amphiboles, varied D_{Ca} between 1 (~12 wt% CaO in melt ≈ basalt; Figure 8) to 6 (~2 wt% CaO ≈ dacite) and compared the calculated trace elements to a database of 290 lavas from Grenada and the Grenadines. The best match of calculated and natural melt composition came using D_{Ca} = 1.70 (T= 970°C) for all igneous xenolith amphiboles. The corresponding CaO in the melt is 7±0.5 wt%, which equates to andesite lavas of this segment of the Lesser Antilles arc (Figure 8), and accords with the upper end of the compositional range of melt inclusions in the igneous xenoliths (i.e. 2.2 to 6.8 wt% CaO; Supplementary Table A3). For the five igneous xenoliths (PSV3, PSV12, PSV14, PSV19, PSV20) the calculated average trace element patterns (Figure 15) show a remarkable match to a trachyandesite (PM2b) and dacite (PM2a) from the adjacent island of Petite Martinique (Figure 2). No comparable match could be obtained for any other of the 290 lavas, giving us confidence that the amphiboles in the xenoliths crystallised from melts of this approximate composition. To further illustrate this point we show also in Figure 14 a typical andesite (GR5) from Grenada. Here the lower LREE and Pb are distinct from Petite Martinique lavas, and appreciably lower than those calculated for all reasonable values of D_{Ca}. For comparison, it is worth noting that the near-liquidus mineralogy of H_2O-saturated, compositionally-similar andesite (P1R) from the island of Martinique at 930 °C, 227 MPa, NNO+2 (Martel et al., 1999) is plagioclase (An_{82}) + amphibole + clinopyroxene + magnetite, in good agreement with the mineralogy of Petit St. Vincent igneous xenoliths (Figure 3).

Although Figure 14 provides a valuable constraint on the broad chemical character of the melts responsible for the igneous xenoliths, it does not satisfactorily explain the observed spread of trace element concentrations, or the distinctive behaviour of U, Th and Sr, and the

tendency of amphibole rims to be more trace element-depleted than their cores (Figure 10c). These features point to additional processes operating on the igneous xenoliths.

Incongruent fractional melting

Extreme depletions in highly incompatible elements such as U and Th, without concomitant variation in less incompatible elements, such as LREE, Sr and Ba cannot be explained by any form of fractional crystallisation without invoking U-Th-rich mineral phases that are not observed in the xenoliths. Conversely, fractional melting can account for this behaviour, as well for the observation that amphibole rims tend to be more depleted than cores. The change in the behaviour of Sr during melting is suggestive of incongruent melting, whereby Sr is released from plagioclase during melting and sequestered by product amphibole, creating a progressive positive Sr anomaly with increasing LREE depletion. To explore these processes, we performed more complex trace element modelling. The main focus of the model was U-Th and Sr-Y ratios as these element pairs best capture the distinctive chemical signature of the igneous amphiboles.

Mathematically, incongruent fractional melting can be approached in a number of formulations. We have used those of Shaw (1979) to calculate for each trace element, *i*, the composition of amphibole (C_{amph}) in equilibrium with incrementally extracted fractional melt:

$$\frac{C^i_{amph}}{C^i_0} = \frac{D^i_{amph}}{D^i_0}\left(1 - \frac{FP^i}{D^i_0}\right)^{\left(\frac{1}{P^i}-1\right)} \qquad (4)$$

Where F is melt fraction, and for each i C_0 is initial concentration in the source, D is the amph-melt partition coefficient, D_0 is the bulk partition coefficient weighted according to mineral abundances in the source, and P is the partition coefficient weighted according to the mineral contribution (p_n) to the melt. For the purposes of our calculations we use a single

melting reaction of the form $p_1 + p_2 + p_3 = 1$ melt. In the case of incongruent melting the coefficients p_n can be either positive or negative, for phases consumed by and produced by, respectively, the melting reaction.

We used the mineral-melt partition coefficients of Nandedkar et al (2016) for amphibole; for all other phases of interest (clinopyroxene, plagioclase) we express their mineral-melt Ds relative to those of amphibole, i.e. $D_{cpx/amph}$ and $D_{plag/amph}$. Weight fractions of amphibole, clinopyroxene and plagioclase in the source are denoted X_{amph}, X_{cpx}, X_{plag}; their contributions to the melt are denoted p_{amph}, p_{cpx}, p_{plag}. In the absence of orthopyroxene from the igneous xenoliths we do not consider this mineral in our calculations. Similarly, we do not consider magnetite because of its low abundance and negligible contribution to the partitioning behaviour of any of the incompatible trace elements considered. Hence $X_{amph} + X_{cpx} + X_{plag} = 1$, and C_0 can be expressed as:

$$C_0^i = C_{amph}^i\left(X_{amph}^i + X_{cpx}^i \cdot D_{cpx/amph}^i + X_{plag}^i \cdot D_{plag/amph}^i\right) \qquad (5a)$$

D_0 can be expressed as:

$$D_0^i = D_{amph}^i\left(X_{amph}^i + X_{cpx}^i \cdot D_{cpx/amph}^i + X_{plag}^i \cdot D_{plag/amph}^i\right) \qquad (5b)$$

and P can be expressed as:

$$P^i = D_{amph}^i\left(p_{amph}^i + p_{cpx}^i \cdot D_{cpx/amph}^i + p_{plag}^i \cdot D_{plag/amph}^i\right) \qquad (5c)$$

Values of $D_{cpx/amph}$ were taken from analyses of coexisting clinopyroxene and amphibole in igneous xenoliths. For the modelling we adopted average values from xenolith PSV14; for

the REE the $D_{cpx/amph}$ values were smoothed (≤10% relative) to yield a variation with ionic radius consistent with the lattice strain model of clinopyroxene-melt partitioning (Wood and Blundy, 1997). For plagioclase we obtained $D_{plag\text{-}melt}$ using the equations of Dohmen and Blundy (2014) at the temperature of interest with the following values: An_{85} plagioclase, $D_{Ca}/D_{Na} = 5$. Note that D_{Ca} is obtained from the ratio of CaO in plagioclase divided by that in melt at the temperature of interest according to Equation (2a). For La we set $D_{plag/amph}$ to the value observed for plagioclase-amphibole pairs in PSV14; for all other REE D_{plag} was determined by the lattice strain model of Dohmen and Blundy (2014). For Eu we assumed that 85% of Eu was present as Eu^{3+} and 15% as Eu^{2+} using the lattice strain approach of Aigner-Torres et al (2007) to calculate the weighted mean D_{Eu}. $D_{plag/amph}$ is then obtained by dividing D_{plag} by D_{amph} as calculated from equation (1). For the source we set X_{amph}, X_{cpx} and X_{plag} to typical values for the igneous xenoliths, i.e. 0.30, 0.44 and 0.26 respectively (Figure 3). The full set of modelling parameters is given in Table 3.

We adopted PSV19_ hblCl7 (Supplementary Table A1 and A4) as the composition of the least-depleted initial amphibole, i.e. C_{amph} in equation (5a). Thus, the only unknown variables in Equation (4) are F, which can be varied systematically, and p. Textural evidence presented above indicates that the incongruent melting reaction proceeds by the addition of hydrous fluids to gabbroic protoliths, melting plagioclase and clinopyroxene to form amphibole and melt. Thus, p_{amph} is negative and p_{cpx} and p_{plag} are positive. We can estimate the magnitude of p_{amph}, p_{cpx} and p_{plag} from the 5 kbar H_2O-saturated melting experiments of (Helz, 1973, Helz, 1976) on a 1921 Kilauea tholeiite. We do this by comparing her run product modes with the anhydrous mineral assemblage of the starting material. The latter was calculated by mass balance, using the mineral compositions in Yoder and Tilley (1962), i.e. 32% clinopyroxene, 12% olivine (Fo_{84}), 45% plagioclase (An_{50}) and 7% magnetite. The differences in phase proportions between run products and starting materials then yields the

stoichiometry of the net H_2O-fluxed melting reaction at the temperature of interest, i.e. the effect of adding H_2O-rich fluid to a hot dry gabbro. The H_2O-saturated solidus for this composition is 690°C (Helz, 1976). For the temperatures of interest of Petit St. Vincent xenoliths (850-1000 °C; Table 3), Helz's experiments yield the following reactions, normalised to 1 mass unit of melt ('ox' denotes magnetite + ilmenite):

825°C 1.8 cpx + 0.6 oliv + 0.4 ox + 2.3 plag = 4.2 amph + 1 melt

875°C 1.2 cpx + 0.5 oliv + 0.3 ox + 1.8 plag = 2.9 amph + 1 melt

930°C 0.7 cpx + 0.3 oliv + 0.2 ox + 1.5 plag = 1.8 amph + 1 melt

970°C 0.6 cpx + 0.2 oliv + 0.2 ox + 1.3 plag = 1.4 amph + 1 melt

Using the same approach, broadly similar values were obtained from the 2 kbar water-saturated experiments of Koepke et al. (2004) on a mid-ocean ridge olivine gabbro, albeit with the additional involvement of orthopyroxene. Although the exact melting conditions and starting compositions for Petit St. Vincent igneous xenoliths will differ from those of Helz's experiments, the overall stoichiometry of her flux-melting reactions (i.e. positive $p_{plag} > 2p_{cpx}$ and negative p_{amph}) is consistent both with textural evidence and the trace element patterns in amphibole. Thus, rather than attempt to parameterise the flux-melting reaction coefficients, for all calculations we adopted a fixed stoichiometry lying within the overall range presented above, but excluding olivine and oxides for simplicity:

1.3 cpx + 2.2 plag = 2.5 amph + 1 melt (6)

Our modelling does not preclude the involvement of olivine and oxides (±orthopyroxene), as seen experimentally, but these phases are either too low in abundance in Petit St. Vincent xenoliths or too poor in the modelled trace elements to materially affect the results.

Using reaction (6) to model the impact of melting on amphibole trace element compositions, we focussed on the distinctive behaviour of U-Th and Sr-Y, specifically the increase in Th/U with decreasing Th (Figure 15a) and increasing Sr/Y with decreasing Y (Figure 15b). For U-Th equations (3a) and (3b) show an increase in D_{Th} with decreasing temperature, and a cross-over from $D_{Th}/D_{U}>1$ to <1 at 810 °C. This change in D_{Th}/D_{U} is critical to explain the U-Th behaviour of the igneous amphiboles, whereby Th/U increases as melting proceeds. We varied temperature to obtain the best fit. We find that a range of values from 970 to 850 °C can account for the observed span in amphibole Th/U and Th concentration, suggesting that the igneous xenoliths experienced melting over this range of temperatures, consistent with amphibole-plagioclase thermometry (Table 2. The lowest temperatures correspond to PSV20 (Figure 3b), while the highest temperatures correspond to primitive xenolith PSV3 (Figure 3a).

By extension to the entire trace element suite, we can then calculate the amphibole trace element patterns produced by melting reaction (6). Results of these calculations, for two representative pairs of temperature and *F* are shown in Figure 16a and compared to selected igneous amphibole rim analyses. The calculated behaviour is an excellent match to that seen in the entire igneous amphibole suite (Supplementary Figure A3, Table A4), except for K and Rb at the highest melt fractions modelled. The good match constitutes an independent test of the proposed melting reaction. The total degree of fractional melting required to explain the data is ≤ 20% (Figure 17 a, b). A striking feature of the calculated trace element behaviour is the development of a strong positive Sr anomaly in PSV20 amphiboles as a result of a high

degree of partial melting (~20%) close to the point of plagioclase exhaustion. At that point the Sr content (and Sr/Y ratio) of the amphibole (and coexisting partial melt) is maximised. Higher degrees of partial melting of PSV20 are consistent with the lower modal abundance of plagioclase in this xenolith (Figure 2) and the rimward increase in An content of plagioclases described above.

Melting reaction (6) describes relatively high-temperature (850-970 °C) flux-melting of a hornblende gabbro protolith whereby addition of H_2O-rich fluid drives incongruent melting by consuming plagioclase and clinopyroxene (positive p_{plag} and p_{cpx}) and producing amphibole (negative p_{amph}). We do not explicitly model the addition of fluid on the assumption that the added fluid does not contribute to the overall trace element budget. However, as the added fluid is unlikely to be pure H_2O, it will make some contribution to the overall budget of elements, in particular highly soluble chlorine and alkalis, including Rb and K. H_2O is dissolved in product melt, as well as incorporated into product amphibole in reaction (6). As the total H_2O content of these phases is just a few weight percent, so the stoichiometric coefficient of H_2O on the left hand side (p_{H2O}) will be small compared to p_{plag} and p_{cpx}.

Origin and evolution of meta-igneous xenoliths

The greater chemical variability of the amphiboles in meta-igneous xenoliths (Figure 10d; Supplementary Figure A3) warrants a slightly different approach. Calculations using the amphibole-melt *D*s of Nandedkar et al. (2016) for a range of plausible D_{Ca} values did not yield a good match for any meta-igneous amphibole to any known lava erupted in the Grenadines or Grenada. The observation suggests that these xenoliths may be of exotic origin, as proposed by White *et al.*, (2017) for hornfelsed meta-igneous xenoliths from Grenada. Possible protoliths include fragments of older arc crust, or vestiges of the over-

riding Caribbean plate (e.g. Allen *et al*., 2019). Alternatively, the meta-igneous xenoliths may have been initially amphibole-free, in which case all amphibole is produced by reactions such as (6) and was never precipitated directly from magmas erupted in the Grenadines.

Despite the lack of a suitable parental magma match to the xenoliths of the meta-igneous suite we can, nonetheless, perform fractional melting calculations to shed light on magmatic processes that shaped the meta-igneous suite. The approach we have taken is similar to that described above. Although orthopyroxene is a minor, relict constituent of some meta-igneous xenoliths we have again chosen not to include it in the calculations as it has very little influence on the results. $D_{cpx/amph}$ are taken from xenolith PSV10, again smoothed in accordance with the lattice strain model for REE. We adopted the same approach to $D_{plag/amph}$ as for the igneous suite, but with An_{50} to reflect the less calcic plagioclase rims in the meta-igneous xenoliths (Figure 5). The starting phase proportions are not well constrained by the xenoliths themselves due to extensive re-equilibration and amphibolitisation. We have adopted an approximately 50:50 mixture of plagioclase (X_{plag} = 0.52) and clinopyroxene (X_{cpx} = 0.44) with very minor amphibole (X_{amph} = 0.04), consistent with gabbro xenoliths found elsewhere in the Lesser Antilles (Melekhova et al. 2019). However, a wide range of amphibole-free starting modes (±orthopyroxene or olivine) works equally well. The dearth of amphibole in the protolith is consistent with textural relationships of the meta-igneous xenoliths (Figure 4) indicating that amphibole formation tends to be late and associated with deformation and melting rather than primocrystic. We used reaction (6) to describe melting stoichiometry. All parameters used for geochemical modelling are provided in Table 3.

As for the igneous xenoliths, we started with the U-Th and Sr-Y systematics. The Th/U ratios of the least-depleted igneous and meta-igneous xenoliths are similar (Figure 15a), indicating that that this ratio was consistent between the protoliths of the two xenolith types. Conversely, the Sr/Y ratio of the meta-igneous xenoliths is lower than that of the igneous

xenoliths (Figure 15b), consistent with a different protoloith for the two xenolith types. PSV8 appears to have characteristics intermediate between the two protoliths, as deduced previously from its distinctive mineral chemistry (Figures 9 to 12). We therefore took as the starting point for the meta-igneous xenolith calculations the least depleted meta-igneous amphibole PSV6_hbl7.

In contrast to the igneous amphiboles, meta-igneous amphiboles show decreasing Th/U with decreasing Th (Figure 15a) and modest increase in Sr/Y with decreasing Y (Figure 15b). The former observation requires a higher D_{Th} and a different sense of U-Th fractionation, i.e. $D_{Th}/D_U>1$, than for the igneous xenoliths. Equations (3a) and (3b) show that both requirements can be met with lower melting temperatures, in accordance with the lower temperatures for meta-igneous xenoliths from thermometry (Table 2); a value of 800 °C best fits the data. The calculated trace element behaviour produced by low-temperature flux-melting reaction (6) is shown for U-Th and Sr-Y in Figure 15a and b respectively. The estimated melt fraction is ≤10%. Modelled trace element patterns for two representative values of *F* are plotted in Figure 16b alongside two additional amphiboles from PSV6 for comparison. As for the igneous amphiboles the calculated behaviour provides a very good match to the amphibole data, except for Pb, where we do not reproduce the strong negative anomaly in the most depleted amphiboles. It is unclear if this reflects uncertainty in D_{Pb} for amphibole (Supplementary Figure A5), or crystallisation of another phase, such as sulfide, that sequesters Pb.

Crustal melting in hot zones

Thermal and experimental modelling show that magmatic underplating at the base of the crust significantly modifies crustal thermal structure and mechanical properties, enhancing deformation and strain localization in an extensional environment (Corti *et al.*, 2003, Furlong

and Fountain, 1986, Fyfe, 1992, Gans, 1987, White and Mawer, 1992, Wilshire, 1990). EBSD analyses of Petit St. Vincent xenoliths have also shown that metasomatic reactions and deformation were contemporaneous and enhanced by fluid addition. Van Rijsingen et al. (2021) showed, based on GPS data along the Lesser Antilles arc, small but detectable along-arc extension which is supported by observations of active normal faulting.

Our petrological study of Petit St. Vincent xenolith supports the existence of a 'hot zone' located in the mid to deep arc crust beneath Petit St. Vincent. Such hot zones grow by the incremental emplacement into the crust of mantle wedge-derived hydrous basalt magmas. Differentiation in the hot zone occurs by a combination of crystallisation and melting (Annen *et al.*, 2006). Melting involves unrelated, older overlying and intercalated arc crust, as well as antecedent intrusions that have previously solidified. Beneath Petit St. Vincent the evidence for pre-existing arc crust is limited to some meta-igneous xenoliths; there is no xenolithic evidence for older sialic crust and radiogenic isotope data for the Grenadines indicate little involvement of such material (e.g. White et al 2017). Melting processes involve the addition of both heat and hydrous fluids released by the basalts as they cool and solidify, thus both thermal and chemical (flux) melting occurs over a range of hot zone temperatures. The latter process, also termed percolative reactive flow (Jackson et al., 2018), is evidenced by the modelled trace element evolution of the Petit St. Vincent xenolith suite (Figure 15).

The fluids involved in chemical melting in the hot zone are unlikely to be pure H_2O or H_2O-CO_2 mixtures. Chlorine concentration in melt inclusions (≤0.9 wt%; Supplementary Table A3) is higher than in any other Grenadine island (e.g. Bequia, ≥0.4 wt%, Camejo-Harry *et al.*, 2018), but similar to Grenada itself, 1.1 to 2.6 wt% (Bouvier *et al.*, 2010). Chlorine concentrations in Petit St. Vincent meta-igneous amphiboles are higher than those in igneous xenoliths at a given K_2O content, but decrease with increasing degree of deformation and metasomatism (Figure 7b). Similarly, concentrations of Li (Figure 12b), Pb and Rb

(Supplementary Figure A3) in meta-igneous minerals are both high and variable. Thus, melt inclusions and mineral chemistry in both igneous and meta-igneous xenoliths, as well as microtextures (Figure 13e) imply the coexistence of Cl-bearing hydrous fluids.

Further evidence for melting of basaltic lithologies comes from the very high anorthite content of plagioclase, up to An_{100} in some xenoliths. Calcic plagioclase is common in arcs (e.g. Danyushevsky *et al.*, 1997, Melekhova *et al.*, 2017, Panjasawatwong *et al.*, 1995, Ushioda *et al.*, 2014) and the Lesser Antilles is no exception (Arculus and Wills, 1980). The origin of very calcic plagioclase ($An \geq 95$) has long been debated, as it is hard to reconcile with any crystallisation process from basaltic magmas with realistic CaO and Na_2O contents. An alternative explanation is H_2O-fluxed fractional melting of plagioclase-bearing gabbros or cumulate rocks, which is inferred from the textures and trace element signatures of Petit St. Vincent xenoliths. Such a process results in very high An plagioclase by simultaneously reducing the liquidus temperature and sequestering Na into the melt. Our trace element modelling (Figure 15b) shows that this process also leads to extreme Sr enrichments in melts just prior to plagioclase exhaustion, the point at which the An content of residual plagioclase is maximised.

Thermal modelling

To explore the above processes in light of the Petit St. Vincent xenolith data we have run numerical simulations in which hydrous basalt (4.5 wt% H_2O) sills are emplaced into arc crust (Annen *et al.*, 2006). We consider two varieties of arc crust. In the first case we consider amphibolitic crust that melts via dehydration melting, as previously modelled by Annen *et al*. (2006). In the second case we consider basaltic crust that has the same composition and H_2O content as the input basalt. This simulates the process of H_2O-fluxed melting because 4.5 wt% is much more H_2O than could be stored sub-solidus in a crustal

rocks. Thus our models capture the two extremes of crustal melting envisaged; thermal melting (heating of crust) and chemical melting (addition of H_2O to hot crust). The melting relationships of hydrous basalt magma and amphibolite crust are shown in Supplementary Figure A5; no account of changing temperature-melt fraction (*T-F*) relationships with pressure is taken. Other constraints for the thermal model are similar to Melekhova *et al.* (2013). We estimated the thickness of pre-existing crust of 10 km based on the thickness of Grenada Basin crust (Christeson *et al.*, 2008). Sills were emplaced randomly between 8 and 12 km depth. Random sill emplacement allows for screens of older crust, such as represented by some meta-igneous xenoliths, to become trapped.

The model was tested with different rates of sill emplacement. We best reproduce the observations in terms of temperature, melting degree, and final crust thickness by emplacing one 300 m basalt sill every 60 kyr over 3.8 Myr. This corresponds to a net rate of crustal growth of 5 km/Myr and results in a crustal thickening of 19 km in agreement with the current depth to the Moho of 29 km (Melekhova et al. 2019). Jicha and Jagoutz (2015) estimate that the magma production rate in the Lesser Antilles arc is 162 km^3 per Myr per km of arc. Thus, for a hot zone with a 40 km^2 footprint beneath Petit St. Vincent (the approximate dimensions of the bathymetric anomaly beneath the archipelago; Figure 1), the total crustal thickening rate is addition is just over 4 km/Myr comparable to the modelled value. We do not track the evolution of fluids exsolved during basalt crystallisation, to the extent that H_2O is conserved at all depths within the model. Thus, we simulate flux melting simply by reheating solidified basaltic crust in the presence of 4.5 wt% H_2O. In nature we would expect significant H_2O-rich fluid migration through the hot zone driving remelting of hot, but dry crustal layers. However, this process is not amenable to simple modelling with fixed *T-F* relationships.

Model results are presented in Figure 17. The initial geotherm at the onset of hot zone development is shown in Figure 17a. The temperature close to the top of the hot zone, at a depth of ~13 km reaches ~950 °C, consistent with igneous xenolith thermometry (Table 2). After 3.8 Myr of sill emplacement the geotherm is perturbed to higher temperatures (Figure 17b). Re-melting in the hot zone occurs in both the pre-existing amphibolite (meta-igneous) and the antecedent intrusive (igneous) portions. After 3.8 Myr, the dehydration melt fraction in the amphibolitic crust is ≤0.12, which is less than that of the surrounding basaltic sills (Figure 17c). Conversely, for the case of basaltic crust, the fluxed melt fraction is ≤0.25 (Figure 17d), which is, by definition, identical to that of the surrounding basaltic sills due to their same *T*-*F* relationships (Supplementary Figure A5). These melt fractions are consistent with the trace element modelling presented in Figure 15, and the overall temperature variation in our modelled hot zone (700-950 °C) matches that recorded by the Petit St. Vincent xenoliths (Table 2) and that inferred from the trace element modelling of U-Th and Sr-Y behaviour (Figure 15). Partial melts of amphibolite crust are predicted to lie at shallower depths (11-21 km) where the temperatures are higher than for the flux melts depths (11-27 km) than meta-igneous crust. Unfortunately, we do not have the requisite pressure resolution for our Petit St. Vincent xenoliths to test this hypothesis.

Overall, our model results demonstrate the greater efficacy of flux melting than dehydration melting, while confirming that both styles of melting are likely to operate in arc hot zones. Note, however, that most melt in the simulations is produced through crystallisation of the basalt sills rather than melting of older crust, albeit this process also likely involves percolative reactive flow of hydrous fluids and melts (Jackson et al., 2018).

CONCLUSIONS

Xenoliths from Petit St. Vincent, Grenadines, provide insights into the construction of sub-arc crust. The presence of metamorphic- and igneous-textured xenoliths evidences the involvement of both older arc crust and antecedent igneous crust. The latter has a protolith composition similar to magmas erupted on the neighbouring island of Petite Martinique, which is possibly part of the same volcanic edifice as Petit St. Vincent (Figure 1), while the former is tentatively ascribed to older, mafic arc crust present at the onset of subduction. Different types of arc magmas are implicated in crustal growth beneath St. Vincent, including representatives of both the C- (ankaramite) and M- (picrite) series magmas erupted on Grenada to the South. An important feature of the xenoliths is the evidence for reworking through the combined addition of heat and hydrous fluids within a crustal section that grows by incremental addition of mantle-derived basaltic magmas. Evidence for crustal reworking includes trace element evolution in xenolith amphiboles that cannot be reconciled with a simple crystallisation history, crystal fabrics indicative of fluid-induced deformation, and the occurrence of very calcic, refractory plagioclase. Thermal models of incremental magma emplacement into the middle crust beneath a 10-km thick layer of older, mafic crust, indicate that the thermal structure and thickness of the sub-arc crust beneath Petit St. Vincent could have developed on a timescale of approximately 4 Ma at rates compatible with the regional arc magma flux. The thermal model successfully replicates xenolith temperatures and dimensions of the arc crust beneath Petit St. Vincent, and supports the reworking of arc crust through repeat magma intrusions. An important aspect of crustal reworking is the operation of both thermal and chemical melting occasioned by the supply of both heat and H_2O-rich fluids from the intruding basalts. Amphibole trace element chemistry from xenoliths can provide a faithful record of these processes, as noted previously by Smith (2014). Based on thermodynamic models and exhumed arc crust sections, Collins *et al.* (2020) have proposed that water-fluxed melting may be an important aspect of sialic arc crust sections world-wide.

The xenoliths from Petit St. Vincent testify to such a process occurring in young, mafic crust beneath an active, intra-oceanic arc.

SUPPLEMENTARY DATA

Supplementary data are available at *Journal of Petrology* online.

DATA AVAILABILITY STATEMENT

All the data underlying this manuscript available in the manuscript and online supplementary material.

ACKNOWLEDGMENTS

We are grateful to S. Kearns and B. Buse for support on the microprobe facilities at the University of Bristol, to R. Robertson, R. Arculus, S. Skora and C. Stamper for field assistance in the Grenadines in 2011, and particularly to M. Diez for bringing our attention to sample PSV10. T. Nagaya is thanked for assistance with the EBSD analysis. We are grateful to E. Chin, A. Kent and an anonymous reviewer for their helpful and constructive comments.

FUNDING

This work was partly funded by ERC Advanced grant 'CRITMAG' 247162 (JB) NERC project 'FAMOS' NE/P017371/1 (JB, FJ), Royal Society Research Professorship RP\R1\201048 (JB) and Commonwealth Scholarship (MC-H). EBSD analyses were supported by JSPS Grant-in-Aid 20KK0079 (SW).

REFERENCES

Allen, R. W., Collier, J. S., Stewart, A. G., Henstock, T., Goes, S., Rietbrock, A. and Team, V. (2019). The role of arc migration in the development of the Lesser Antilles: A new tectonic model for the Cenozoic evolution of the eastern Caribbean. *Geology* **47**, 891-895.

Andersen, D. J. and Lindsley, D. H. (1985). New (and final!) models for the Ti-magnetite/ilmenite geothermometer and oxygen barometer. *Spring Meeting EoS Transactions American Geophysical Union* **66**.

Annen, C., Blundy, J. D. and Sparks, R. S. J. (2006). The Genesis of Intermediate and Silicic Magmas in Deep Crustal Hot Zones. *Journal of Petrology* **47**, 505-539.

Arculus, R. J. and Wills, K. J. A. (1980). The petrology of plutonic blocks and inclusions fromthe Lesser Antilles Island Arc. *Journal of Petrology* **21**, 743-799.

Bachmann, F., Hielscher, R. and Schaeben, H. (2010). Texture analysis with MTEX–free and open source software toolbox. *Solid State Phenomena*: Trans Tech Publ, 63-68.

Ballhaus, C., Berry, R. F. and Green, D. H. (1991). High pressure experimental calibration of the olivine-orthopyroxene-spinel oxygen geobarometer: implications for the oxidation state of the upper mantle. *Contributions to Mineralogy and Petrology* **107**, 27-40.

Barth, M. G., McDonough, W. F. and Rudnick, R. L. (2000). Tracking the budget of Nb and Ta in the continental crust. *Chemical Geology* **165**, 197-213.

Bergantz, G.W. (1995) Changing techniques and paradigms for the evaluation of magmatic processes. *Journal of Geophysical Research,* **100**, B9, 17603-17613

Bezard, R., Davidson, J. P., Turner, S., Macpherson, C. G., Lindsay, J. M. and Boyce, A. J. (2014). Assimilation of sediments embedded in the oceanic arc crust: myth or reality? *Earth and Planetary Science Letters* **395**, 51-60.

Blundy, J. and Cashman, K. (2008). Petrologic Reconstruction of Magmatic System Variables and Processes. *Reviews in Mineralogy and Geochemistry* **69**, 179-239.

Bouvier, A. S., Métrich, N. and Deloule, E. (2010). Light elements, volatiles, and stable isotopes in basaltic melt inclusions from Grenada, Lesser Antilles: Inferences for magma genesis. *Geochemistry, Geophysics, Geosystems* **11**.

Bouysse, P. and Westercamp, D. (1990). Subduction of Atlantic aseismic ridges and Late Cenozoic evolution of the Lesser Antilles island arc. *Tectonophysics* **175**, 349-380.

Bouysse, P., Westercamp, D. and Andreieff, P. (1990). The Lesser Antilles Island Arc. In: Moore, J. C., Mascle, A., Taylor, E., Alvarez, F., Andreieff, P., Barnes, R., Beck, C., Behrmann, J. H., Blanc, G., Brown, K. M., Clark, M. W., Dolan, J. F., Fisher, A. T., Gieskes, J. M., Hounslow, M. W., McLellan, P., Moran, K., Ogawa, Y., Sakai, T., Schoonmaker, J., Vrolijk, P. J., Wilkens, R., Williams, C. and Winkler, W. R. (eds.) *Proceedings of the Ocean Drilling Program, Scientific Results*. College Station, TX: Ocean Drilling Program, 29-44.

Burg, J., Bodinier, J., Chaudhry, S., Hussain, S. and Dawood, H. (1998). Infra-arc mantle-crust transition and intra-arc mantle diapirs in the Kohistan Complex (Pakistani Himalaya): petro-structural evidence. *Terra Nova-Oxford* **10**, 74-80.

Braszus, B., Goes. S., Allen, R., Rietbrock, A., Collier, J., Harmon, N., Henstock, T., Hicks, S., Rychert, C. A., Maunder, B., van Hunen, J., Bie, L., Blundy, J., Cooper, G., Davy, R., Kendall, M., Macpherson, C., Wilkinson, J., Wilson, M. (2021) Subduction history of the Caribbean from uppermantle seismic imaging and plate reconstruction. *Nature Communication,* **12**, 4211.

Butt, A. J. (2012). Characterising deformation beneath an arc volcano: insights from Petit St. Vincent, Lesser Antilles. *Department of Earth Sciences*. United Kingdom: University of Bristol.
Camejo-Harry, M., Melekhova, E., Blundy, J., Attridge, W., Robertson, R. and Christopher, T. (2018). Magma evolution beneath Bequia, Lesser Antilles, deduced from petrology of lavas and plutonic xenoliths. *Contributions to Mineralogy and petrology* **173**, 1-26.
Cashman, K. V., Sparks, R. S. J. and Blundy, J. D. (2017). Vertically extensive and unstable magmatic systems: A unified view of igneous processes. *Science* **355**.
Christeson, G., Mann, P., Escalona, A. and Aitken, T. J. (2008). Crustal structure of the Caribbean–northeastern South America arc-continent collision zone. *Journal of Geophysical Reasearch* **113**, B08104.
Collins, W. J., Murphy, J. B., Johnson, T. E. and Huang, H.-Q. (2020). Critical role of water in the formation of continental crust. *Nature Geoscience* **13**, 331-338.
Cooper G., Macpherson, C.G., Blundy, J.D., Maunder, B., Allen, R.W., Goes, S., Collier, J.S., Bie, L, Harmon, N., Hicks, S.P., Iveson, A.A., Prytulak, J., Rietbrock, A., Rychert, C.A., Davidson, J.P. & the VoiLA team (2020). Variable water input controls evolution of the Lesser Antilles volcanic arc. *Nature* **582.**
Corti, G., Bonini, M., Conticelli, S., Innocenti, F., Manetti, P. and Sokoutis, D. (2003). Analogue modelling of continental extension: a review focused on the relations between the patterns of deformation and the presence of magma. *Earth-Science Reviews* **63**, 169-247.
Danyushevsky, L. V., Carroll, M. R. and Falloon, T. J. (1997). Origin of high-An plagioclase in Tongan high-Ca boninites: implications for plagioclase melt equilibria at low P (H∼ 2O). *Canadian Mineralogist* **35**, 313-326.
Davidson, J. (1985). Mechanisms of contamination in Lesser Antilles island arc magmas from radiogenic and oxygen isotope relationships. *Earth and Planetary Science Letters* **72**, 163-174.
DeBari, S., Kay, S. M. and Kay, R. (1987). Ultramafic xenoliths from Adagdak volcano, Adak, Aleutian Islands, Alaska: deformed igneous cumulates from the Moho of an island arc. *The Journal of Geology* **95**, 329-341.
DeBari, S. M. and Greene, A. R. (2011). Vertical stratification of composition, density, and inferred magmatic processes in exposed arc crustal sections. *Arc-continent collision*: Springer, 121-144.
Deer, W. A., Howie, R. A. and Zussman, J. (2013). *An Introduction to the Rock-Forming Minerals*. London: The Mineralogical Society.
Dohmen, R. and Blundy, J. (2014). A predictive thermodynamic model for element partitioning between plagioclase and melt as a function of pressure, temperature and composition. *American Journal of Science* **314**, 1319-1372.
Droop, G. T. R. (1987). A general equation for estimating Fe3+ concentrations in ferromagnesian silicates and oxides from microprobe analyses, using stoichiometric criteria. *Mineralogcal Magazine* **51**, 431-435.
Furlong, K. P. and Fountain, D. M. (1986). Continental crustal underplating: Thermal considerations and seismic‐petrologic consequences. *Journal of Geophysical Research: Solid Earth* **91**, 8285-8294.
Fyfe, W. (1992). Magma underplating of continental crust. *Journal of Volcanology and Geothermal Research* **50**, 33-40.
Gans, P. B. (1987). An open‐system, two‐layer crustal stretching model for the eastern Great Basin. *Tectonics* **6**, 1-12.

Ghiorso, M. S. and Evans, B. W. (2008). Thermodynamics of Rhombohedral Oxide Solid Solutions and a Revision of the Fe-Ti Two-oxide Geothermometer and Oxygen-barometer. *American Journal of Science* **308**, 957-1039.
Helz, R. T. (1973). Phase relations of basalts in their melting range at PH2O= 5 kb as a function of oxygen fugacity: part I. Mafic phases. *Journal of Petrology* **14**, 249-302.
Helz, R. T. (1976). Phase relations of basalts in their melting ranges at P H2O= 5 kb. Part II. Melt compositions. *Journal of Petrology* **17**, 139-193.
Hildreth, W., & Moorbath, S. (1988). Crustal contributions to arc magmatism in the Andes of central Chile. *Contributions to mineralogy and petrology*, *98*(4), 455-489.
Holland, T. and Blundy, J. (1994). Non-ideal interactions in calcic amphiboles and their bearing on amphibole-plagioclase thermometry. *Contributions to Mineralogy and Petrology* **116**, 433-447.
Humphreys, M. C. S., Kearns, S. L. and Blundy, J. D. (2006). SIMS investigation of electron-beam damage to hydrous, rhyolitic glasses: implications for melt inclusion analysis. *American Mineralogist* **91**, 667-679.
Jackson M.D., Blundy, J. & Sparks R.S.J. (2018). Chemical differentiation, cold storage and remobilization of magma in the Earth's crust. *Nature* **564**, 7736
Jagoutz, O. (2014). Arc crustal differentiation mechanisms. *Earth and Planetary Science Letters* **396**, 267-277.
Jagoutz, O. and Kelemen, P. B. (2015). Role of arc processes in the formation of continental crust. *Annual Review of Earth and Planetary Sciences* **43**, 363-404.
Jicha, B. R. and Jagoutz, O. (2015). Magma production rates for intraoceanic arcs. *Elements* **11**, 105-111.
Jenner, F. E., & O'Neill, H. S. C. (2012). Major and trace analysis of basaltic glasses by laser-ablation ICP-MS. *Geochemistry, Geophysics, Geosystems*, ***13***(3).
Kay, S. M. and Kay, R. W. (1985). Role of crystal cumulates and the oceanic crust in the formation of the lower crust of the Aleutian arc. *Geology* **13**, 461-464.
Kodaira, S., T. Sato, Takahashi, N., Ito, A., Tamura, Y., Tatsumi, Y. and Kaneda, Y. (2007). Seismological evidence for variable growth of crust along the Izu intraoceanic arc. *Journal of Geophysical Reasearch* **112**, B05104.
Koepke, J., Feig, S. T., Snow, J. and Freise, M. (2004). Petrogenesis of oceanic plagiogranites by partial melting of gabbros: an experimental study. *Contributions to Mineralogy and petrology* **146**, 414-432.
Kouzmanov, K., Pokrovski, G. S., Hedenquist, J., Harris, M. and Camus, F. (2012). Hydrothermal controls on metal distribution in porphyry Cu (-Mo-Au) systems. *Society of Economic Geologists Special Publication* **16**, 573-618.
Leake, B. E., Woolley, A. R., Arps, C. E. S., Birch, W. D., Gilbert, M. C., Grice, J. D., Hawthorne, F. C., Kato, A., Kisch, H. J., Krivovichev, V. G., Linthout, K., Laird, J., Mandarino, J. A., Maresch, W. V., Nickel, E. H., Rock, N. M. S., Schumacher, J. C., Smith, D. C., Stephenson, N. C. N., Ungaretti, L., Whittaker, E. J. W. and Youzhi, G. (1997). Nomenclature of amphiboles: Report of the Subcommittee on Amphiboles of the Interational Mineralogical Association, Commission on New Minerals and Mineral Names. *The Canadian Mineralogist* **35**, 219-246.
LePage, L. D. (2003). ILMAT: an Excel worksheet for ilmenite–magnetite geothermometry and geobarometry. *Computers and Geosicences* **29**, 673-678.
Lindsley, D. H. (1983). Pyroxene thermometry. *American Mineralogist* **68**, 477-493.
Lindsley, D. H. and Spencer, K. J. (1982). Fe-Ti oxide geothermometry: Reducing analyses of coexisting Ti-magnetite (Mt) and ilmenite (Ilm). *EoS Transactions, American Geophysical Union* **63**, 471.

Macdonald, R., Hawkesworth, C. J. and Heath, E. (2000). The Lesser Antilles volcanic chain: a study in arc magmatism. *Earth-Science Reviews* **49**, 1-76.
Melekhova, E., Annen, C. and Blundy, J. (2013). Compositional gaps in igneous rock suites controlled by magma system heat and water content. *Nature Geoscience* **6**, 385-390.
Melekhova, E., Blundy, J., Martin, R., Arculus, R. and Pichavant, M. (2017). Petrological and experimental evidence for differentiation of water-rich magmas beneath St. Kitts, Lesser Antilles. *Contributions to Mineralogy and petrology* **172**, 98.
Melekhova, E., Schlaphorst, D., Blundy, J., Kendall, J.-M., Connolly, C., McCarthy, A. and Arculus, R. (2019). Lateral variation in crustal structure along the Lesser Antilles arc from petrology of crustal xenoliths and seismic receiver functions. *Earth and Planetary Science Letters* **516**, 12-24.
Miyake, A., Takigawa, A., Igami, Y., Ohi, S., Nakamura, R., Tsuchiyama, A. (2016). Inconsistency between SEM image and Crystal orientation data obtained by SEM- EBSD systems . *JpGU Meeting 2016*. Japan.
Nandedkar, R. H., Hürlimann, N., Ulmer, P. and Müntener, O. (2016). Amphibole–melt trace element partitioning of fractionating calc-alkaline magmas in the lower crust: an experimental study. *Contributions to Mineralogy and petrology* **171**, 1-25.
Nandedkar, R. H., Ulmer, P. and Müntener, O. (2014). Fractional crystallization of primitive, hydrous arc magmas: an experimental study at 0.7 GPa. *Contributions to Mineralogy and petrology* **167:1015**.
Otamendi, J. E., Ducea, M. N. and Bergantz, G. W. (2012). Geological, petrological and geochemical evidence for progressive construction of an arc crustal section, Sierra de Valle Fertil, Famatinian Arc, Argentina. *Journal of Petrology* **53**, 761-800.
Palme, H. and O'Neill, H. S. C. (2003). Cosmochemical estimates of mantle composition. *Treatise on geochemistry* **2**, 568.
Panjasawatwong, Y., Danyushevsky, L. V., Crawford, A. J. and Harris, K. L. (1995). An experimental study of the effects of melt composition on plagioclase - melt equilibria at 5 and 10 kbar: implications for the origin of magmatic high-An plagioclase. *Contributions to Mineralogy and petrology* **118**, 420-432.
Paton, C., Hellstrom, J., Paul, B., Woodhead, J. and Hergt, J. (2011). Iolite: Freeware for the visualisation and processing of mass spectrometric data. *Journal of Analytical Atomic Spectrometry* **26**, 2508-2518.
Plank, T. and Langmuir, C. H. (1993). Tracing trace elements from sediment input to volcanic output at subduction zones. *Nature* **362**, 739-743.
Plank, T. and Langmuir, C. H. (1998). The chemical composition of subducting sediment and its consequences for the crust and mantle. *Chemical Geology* **145**, 325-394.
Putirka, K. D. (2008). Thermometers and barometers for volcanic systems. *Reviews in Mineralogy and Geochemistry* **69**, 61-120.
Rojas-Agramonte, Y., Williams, I. S., Arculus, R., Kröner, A., García-Casco, A., Lázaro, C., Buhre, S., Wong, J., Geng, H. and Echeverría, C. M. (2017). Ancient xenocrystic zircon in young volcanic rocks of the southern Lesser Antilles island arc. *Lithos* **290**, 228-252.
Rudnick, R., Gao, S., Holland, H. and Turekian, K. (2003). Composition of the continental crust. *The crust* **3**, 1-64.
Rudnick, R. L. (2018). Earth's Continental Crust. In: White, W. M. (ed.) *Encyclopedia of Geochemistry: A Comprehensive Reference Source on the Chemistry of the Earth*. Cham: Springer International Publishing, 392-418.

Satsukawa, T., Ildefonse, B., Mainprice, D., Morales, L. F. G., Michibayashi, K., and Barou, F. (2013). A database of plagioclase crystal preferred orientations (CPO) and microstructures – implications for CPO origin, strength, symmetry and seismic anisotropy in gabbroic rocks. *Solid Earth* **4,** 511–542, https://doi.org/10.5194/se-4-511-2013.
Schlaphorst, D., Melekhova, E., Kendall, J.-M., Blundy, J. and Latchman, J. L. (2018). Probing layered arc crust in the Lesser Antilles using receiver functions. *Royal Society Open Science* **5**.
Shaw, D. M. (1979). Trace element melting models. *Physics and Chemistry of the Earth* **11**, 577-586.
Schlaphorst, D., Harmon, N., Kendall, J. M., Rychert, C. A., Collier, J., Rietbrock, A., ... & VoiLA Team. (2021). Variation in upper plate crustal and lithospheric mantle structure in the greater and Lesser Antilles from ambient noise tomography. *Geochemistry, Geophysics, Geosystems*, **22**(7), e2021GC009800.
Shillington, D. J., Van Avendonk, H. J., Behn, M. D., Kelemen, P. B. and Jagoutz, O. (2013). Constraints on the composition of the Aleutian arc lower crust from VP/VS. *Geophysical Research Letters* **40**, 2579-2584.
Smith, D. J. (2014). Clinopyroxene precursors to amphibole sponge in arc crust. *Nature Communications*, ***5***(1), 1-6.
Spiess, R., Dibona, R., Faccenda, M., Mattioli, M. and Renzulli, A. (2017). Mylonitic gabbro nodules of Stromboli (southern Italy): Microstructural evidence of high-temperature deformation of cumulates during the evolution of the magmatic crustal roots of an active volcano. *Geological Society of America Special Papers* **526**, 89-105.
Streckeisen, A. (1976). To each plutonic rock its proper name. *Earth Science Reviews* **12**, 1-33.
Taylor, S. R. and McLennan, S.M. (1995). The geochemical evolution of the continental crust." *Reviews of geophysics* **33**, no. 2, 241-265.
Thirlwall, M. (1991). Long-term reproducibility of multicollector Sr and Nd isotope ratio analysis. *Chemical Geology: Isotope Geoscience Section* **94**, 85-104.
Thirlwall, M. F., Graham, A. M., Arculus, R. J., Harmon, R. S. and Macpherson, C. G. (1996). Resolution of the effects of crustal assimilation, sediment subduction, and fluid transport in island arc magmas: Pb-Sr-Nd-O isotope geochemistry of Grenada, Lesser Antilles. *Geochimica et Cosmochimica Acta* **60**, 4785-4810.
Ulmer, P., Kaegi, R. and Müntener, O. (2018). Experimentally derived intermediate to silica-rich arc magmas by fractional and equilibrium crystallization at 1· 0 GPa: an evaluation of phase relationships, compositions, liquid lines of descent and oxygen fugacity. *Journal of Petrology* **59**, 11-58.
Ushioda, M., Takahashi, E., Hamada, M. and Suzuki, T. (2014). Water content in arc basaltic magma in the Northeast Japan and Izu arcs: an estimate from Ca/Na partitioning between plagioclase and melt. *Earth, Planets and Space* **66**, 1-10.
van Rijsingen, E., Calais, E., Jolivet, R., de Chabalier, J.-B., Robertson, R., Ryan, G. A. and Symithe, S. (2021). Vertical tectonic motions in the Lesser Antilles: linking short-and long-term observations.
Wager, L. R., Brown, G. M. and Wadsworth, W. J. (1960). Types of igneous cumulates. *Journal of Petrology* **1**, 73-85.
Wells, P. R. A. (1977). Pyroxene thermometry in simple and complex systems. *Contributions to Mineralogy and Petrology* **62**, 129-139.
Wallis, S. R., Kobayashi, H., Nishii, A., Mizukami, T., & Seto, Y. (2011). Obliteration of olivine crystallographic preferred orientation patterns in subduction-related antigorite-

bearing mantle peridotite: an example from the Higashi–Akaishi body, SW Japan. *Geological Society, London, Special Publications* **360**(1), 113-127.
White, J. C. and Mawer, C. K. (1992). Deep-crustal deformation textures along megathrusts from Newfoundland and Ontario: implications for microstructural preservation, strain rates, and strength of the lithosphere. *Canadian Journal of Earth Sciences* **29**, 328-337.
White, W., Copeland, P., Gravatt, D. R. and Devine, J. D. (2017). Geochemistry and geochronology of Grenada and Union islands, Lesser Antilles: The case for mixing between two magma series generated from distinct sources. *Geosphere* **13**, 1359-1391.
Wilshire, H. (1990). Lithology and evolution of the crust‐mantle boundary region in the southwestern Basin and Range Province. *Journal of Geophysical Research: Solid Earth* **95**, 649-665.
Wood, B. J. and Blundy, J. D. (1997). A predictive model for rare earth element partitioning between clinopyroxene and anhydrous silicate melt. *Contributions to Mineralogy and petrology* **129**, 166-181.
Wood, B.J., Blundy, J.D. (2001).The effect of cation charge on crystal-melt partitioning of trace elements. *Earth and Planetary Science Letters* **188**, 59-71.
Yamamoto, M., Kagami, H., Narita, A., Maruyama, T., Kondo, A., Abe, S. and Takeda, R. (2013). Sr and Nd isotopic compositions of mafic xenoliths and volcanic rocks from the Oga Peninsula, Northeast Japan Arc: Genetic relationship between lower crust and arc magmas. *Lithos* **162-163**, 88-106.
Yoder, H. S. and Tilley, C. E. (1962). Origin of basalt magmas: an experimental study of natural and synthetic rock systems. *Journal of Petrology* **3**, 342-532.

Table 1. Classification, minerals, crystallisation sequences and descriptions of Petit St. Vincent samples

Sample	Rock name	Texture	ol	plag	cpx	opx	hbl	spl	ilm	ap	Crystallisation sequence	Description
IGNEOUS												
poikilitic hornblende												
PSV 1	pyroxene-hbl gabbro	orthocumulate	-	50	24	-	22	4	-	-	spl/plag, cpx, hbl	medium grained; subhedral, zoned; sieve textured plag; poikilitic hbl; uralitization
PSV 3	pyroxene hornblendite	mesocumulate	-	-	41	-	59	tr	-	-	spl, hbl, cpx, hbl	coarse grained; hbl <5mm; subhedral, zoned
PSV 12	pyroxene-hbl gabbro	mesocumulate	-	50	19	-	30	1	-	tr	spl/plag, cpx, hbl	medium grained; subhedral, zoned; sieve textured plag; uralitization; microcracks; MI
PSV 14	mela pyroxene-hbl gabbro	orthocumulate	tr	28	30	-	42	tr	-	tr	spl/ol, plag, cpx, hbl	medium grained; subhedral, zoned; poikilitic hbl; sieve textured plag; uralitization; resorbed iddingsite; interstitial melt

PSV 19	pyroxene-hbl gabbro	orthocumulate	-	46	26	-	24	4	-	-	spl, plag/cpx, hbl	medium grained; subhedral, zoned; sieve textured plag; poikilitic hbl; uralitization; MI
subhedral hornblende												
PSV 5	pyroxene-hbl gabbro	mesocumulate	-	55	27	-	10	8	-	-	spl/plag, hbl, cpx	coarse grained; hbl <5mm; spl < 2mm; subhedral, zoned; sieve textured plag
PSV 11	pyroxene-hbl gabbro	mesocumulate	-	55	26	-	19	tr	-	-	spl/plag, cpx, hbl	medium grained; subhedral, zoned; sieve textured plag; uralitization; interstitial melt
PSV 20	mela pyroxene-hbl gabbro	adcumulate	-	11	26	-	62	1	-	-	spl, cpx, plag/hbl	coarse grained; hbl <6.5mm; subhedral, zoned; sieve textured plag; prismatic hbl; MI
META-IGNEOUS												
PSV 6	pyroxene-hbl gabbro	granoblastic amoeboid	-	47	13	-	39	tr	1	-	spl, plag, ilm, cpx, hbl, plag/hbl	microcrystalline interspersed with medium grained plag and hbl; subhedral,

												zoned; 2 generations of plag (<3 mm) and hbl (2.5 mm) distinguished by size; sieve textured, sutured contacts plag
PSV 8	pyroxene-hbl gabbro	granoblastic	-	44	38	-	18	-	tr	-	plag/ilm, cpx, hbl	fine grained; ganoblastic; weak foliation; subhedral, zoned; sheared plagioclase; deformed cpx & hbl; microcracks; MI
PSV 10	-	mylonite	-	76	40	-	24	tr	-	-		fine grained; strong foliation; strained porphyroclasts; asymmetric boudinage; deformed cpx & hbl; microcracks
PSV 16	gabbro	phaneritic	-	57	43	-	-	-	tr	tr	plag/ilm, cpx	coarse grained; cpx <7mm, euhedral; plag sieve textured, subhedral, unzoned, deformation twins; crystal

												preferred orientation; microcracks
PSV 17	-	granoblastic	-	x	x	-	x	x	-	-	spl/plag/cpx, hbl	fine grained; ganoblastic; weak foliation; subhedral, zoned; sheared plagioclase; deformed cpx & hbl (trace); microcracks
PSV 18	-	blastoporphyritic	-	x	x	x	x	tr	-	-	spl, plag, cpx, opx, hbl	coarse grained; plag <6mm; sieve textured, sheared plag; deformed cpx; microcracks
HYPABYSSAL												
PSV 13	dolerite	hypabyssal	-	72	22	-	-	6	tr	-	spl/plag, ilm, cpx	medium grained; cpx euhedral, zoned; plag subhedral, zoned, sieve textured; MI
LAVA												
PSV L1b	basalt	glomeroporphyritic	x	x	x	-	-	x	-	-	spl, ol, plag/cpx	medium grained; subhedral, zoned; partially iddingsitized ol; crystal clots

Where no rock name is assigned, samples were not point counted or too deformed/altered to be point counted with sufficient accuracy

Cumulate textural designations (after Wager, Brown, and Wadsworth (1960)) are given for igneous xenoliths

x, mineral phase present but sample was not point counted; -, mineral phase absent; *ol*, olivine; *plag*, plagioclase; *cpx*, clinopyroxene; *opx*, orthopyroxene; *hbl*, hornblende; *spl*, spinel; *ilm*, ilmenite; *ap*, apatite; *MI*, melt inclusion, tr- less than 0.5wt%.

Table 2. Calculated intensive parameters for Petit St. Vincent rocks

Sample	Group	Method	Phases	T (°C)	P (MPa)	ΔNNO
PSVL1	lava	Ballhaus et al. (1991)	ol-spl	1014-1095	*500*	2.65-2.87
PSV13	hypabyssal	(Andersen and Lindsley, 1985)[1]	spl-ilm	936	-	0.5
PSV13		(Ghiorso and Evans, 2008)	spl-ilm	985	-	1.1
PSV13		(Putirka, 2008)	cpx-liq	965	-	-
PSV20	igneous	Holland and Blundy (1994)[2]	hbl-plag	960-971	*500*	-
PSV1				966-1023		-
PSV14				963		-
PSV12				847-1039		-
PSV8	Meta-	Holland and Blundy (1994)[2]	hbl-plag	912-936	*500*	-
PSV6	igneous	(Andersen and Lindsley, 1985)[1]	spl-ilm	803-847	-	1.37-1.77
PSV6		(Ghiorso and Evans, 2008)	spl-ilm	848-883	-	1.48-1.67
PSV6		Holland and Blundy (1994)[2]	hbl-plag	799-874	*500*	-
PSV18		Holland and Blundy (1994)[2]	hbl-plag	790-849	*500*	-
PSV18		(Wells, 1977)	cpx-opx	904-914	-	-
PSV18		(Putirka, 2008)	cpx-opx	910-929	397-457	-

[1]Lindsley and Spencer (1982) oxide formula recalculation

[2][edenite + albite = richterite + anorthite]

500 - assumed pressure

Table 3. Trace elements modelling parameters

Model	Igneous amphiboles			Igneous amphiboles			Meta-igneous amphiboles		
T (°C)	850			970			800		
source mineralogy									
*X*amph	0.30			0.30			0.04		
*X*plag	0.44			0.44			0.52		
*X*cpx	0.26			0.26			0.44		
melting reactions									
*p*amph	-2.50			-2.50			-2.50		
*p*plag	2.20			2.50			2.50		
*p*cpx	1.30			1.00			1.00		
An(plag)	0.85			0.85			0.50		
Kd(plag)	5.00			5.00			5.00		
partition coefficients									
	amph/L	plag/amph	cpx/amph	amph/L	plag/amph	cpx/amph	amph/L	plag/amph	cpx/amph
source	N et al	DB14	PSV14	N et al	DB14	PSV14	N et al	DB14	PSV10
Rb	0.10	0.035	0.010	0.10	0.032	0.010	0.10	0.054	0.010
Ba	0.408	0.219	0.015	0.194	0.526	0.015	0.585	0.282	0.025
Th	0.086	0.046	0.810	0.017	0.237	0.810	0.189	0.021	0.235
U	0.081	0.049	0.850	0.012	0.331	0.850	0.204	0.020	0.466
Nb	0.78	0.005	0.022	0.40	0.010	0.022	1.06	0.004	0.007
Ta	0.59	*0.003*	0.060	0.38	*0.005*	0.060	0.73	0.003	*0.007*
K	0.16	0.339	0.064	0.34	0.109	0.064	0.11	0.629	0.100
La	0.31	0.176	0.708	0.16	0.353	0.708	0.44	0.321	0.147
Ce	0.67	0.064	0.632	0.30	0.146	0.632	0.99	0.102	0.132
Pb	0.30	1.050	0.243	0.07	4.169	0.243	0.60	0.912	0.382
Pr	1.17	0.028	0.641	0.50	0.069	0.641	1.76	0.040	0.139
Sr	0.49	7.04	0.173	0.42	5.25	0.173	0.52	8.96	0.656
Nd	2.04	0.012	0.600	0.83	0.032	0.600	3.14	0.015	0.133
Sm	3.69	0.004	0.646	1.47	0.010	0.646	5.74	0.004	0.153
Zr	1.07	0.001	0.843	0.38	0.003	0.843	1.77	0.001	0.240
Hf	1.67	*0.001*	0.929	0.76	*0.001*	0.929	2.42	0.000	0.165
Eu	4.30	0.135	0.688	1.60	0.233	0.688	6.93	0.112	0.161
Ti	5.66	0.0053	0.430	2.99	0.0100	0.430	7.70	0.0039	0.158
Gd	5.07	0.0015	0.691	2.15	0.0042	0.691	7.68	0.0014	0.177
Tb	5.96	0.0009	0.669	2.38	0.0029	0.669	9.27	0.0008	0.171
Dy	6.20	0.0006	0.702	2.48	0.0020	0.702	9.65	0.0005	0.183
Y	6.14	0.0005	0.725	2.20	0.0019	0.725	10.06	0.0004	0.184
Ho	6.35	0.0005	0.718	2.48	0.0015	0.718	9.99	0.0003	0.189
Er	6.12	0.0003	0.729	2.35	0.0012	0.729	9.71	0.0002	0.198

Tm	5.54	0.0003	0.819	2.24	0.0010	0.819	8.58	0.0002	0.224
Yb	5.23	0.0002	0.841	1.98	0.0009	0.841	8.37	0.0001	0.225
Lu	5.08	0.0002	0.829	1.81	0.0008	0.829	8.35	0.0001	0.217

N et al - Nandedakar et al (2016), DB14 - D(plag/L) from Dohmen & Blundy (2014). Values in italics are estimated or interpolated, cpx/amph values are smoothed to conform to lattice strain model.

FIGURE CAPTIONS

Figure 1. Map showing the topography of the southern part of Lesser Antilles volcanic arc, comprising Grenada, St. Vincent and Grenadines archipelago in between. Kick-'em-Jenny submarine volcano is denoted as a grey triangle. Inset maps show (a) the Lesser Antilles arc; and (b) the location of Petit St. Vincent, Petite Martinique and several small islets that form a circular archipelago. Bathymetry data are from NOAA website.

Figure 2. Modal proportions by mass of minerals in Petit St. Vincent dyke rock, lava and xenoliths with their textural groupings. Xenoliths are listed in order of decreasing plagioclase An content downwards within a texturally defined group. Modes for PSV10 and PSV11 obtained using EBSD imaging; all others from manual point-counting. Note presence of An_{99} plagioclase in mylonitic xenolith PSV10.

Figure 3. Photomicrographs of igneous xenolith textures: (a) Plagioclase-free pyroxene hornblendite (PSV3, PPL-plain polarised light); (b) Prismatic hornblende and sieve-textured plagioclase in mela pyroxene-hornblende gabbro (PSV20, PPL); (c) Sector zoned clinopyroxene and hornblende oikocryst with plagioclase chadacrysts in pyroxene-hornblende gabbro (PSV19, PPL); (d) Foliated pyroxene-hornblende gabbro showing uralitization of clinopyroxene to hornblende and formation of euhedral hornblende (PSV11, PPL); (e) Hornblende-free dolerite with euhedral clinopyroxene and sieve-textured plagioclase (PSV13, PPL); (f) Lava with phenocrysts of partial iddingsitized olivine, zoned clinopyroxene and plagioclase (PSVL1b, XPL- cross polarised light).

Figure 4. Photomicrographs of meta-igneous xenolith textures. Degree of deformation, recyrstallisation and metamorphism increases from (a) to (f). (a) Gabbro with strong crystal preferred orientation of clinopyroxene and plagioclase (PSV16, PPL); (b) Anhedral plagioclase 'megacrysts' in equigranular, microcrystalline groundmass of hornblende + clinopyroxene + plagioclase showing evidence of late-stage coarsening. Microcrystalline

grain edges show interpenetrating contacts (PSV6, PPL); (c) Foliated xenolith with well-developed granoblastic texture and internally-deformed and recrystallized plagioclase domains (PSV8, PPL). Note vertical inter-granular microcrack on right-hand side of image filled with newly formed clinopyroxene and hornblende; (e) Sheared mosaic of plagioclase grains with post-deformation hornblende (PSV18, XPL); (e) Plagioclase 'megacryst' displaying intact core and recrystalised rim (PSV17, XPL); (f) Strongly deformed mylonitic xenolith with clinopyroxene and hornblende porphyroclasts showing evidence of internal strain, such as asymmetric microboudinage, and plagioclase-rich and clinoyroxene-rich domains (PSV10, PPL).

Figure 5. Variation in plagioclase composition in terms of (a) Fe and (b) K atoms per formula unit (pfu) for Petit St. Vincent xenoliths and lava. Meta-igneous xenolith samples shown with open blue symbols; igneous xenoliths with red, filled symbols; dolerite (PSV13) with green, filled circles; and lava (PSVL1b) with black diamonds. Typical analytical uncertainties for Fe and K, based on the counting statistics are 3.2 and 1.5% respectively. Propagated averaged uncertainties on the An number is ± 1.1 mol%. Note progressive evolution of An content of plagioclase in dolerite (PSV13) with change in Fe content indicating differentiation, and negative correlation of Fe with An for majority of meta-igneous xenolith demonstrating solid-state recrystallisation processes. Exceptions are PSV10 and PSV17 that experienced recrystallization during partial melting. Highlighted dark (core) and light blue (rim) diamonds show core-rim evolution in PSV17.

Figure 6. Variation in clinopyroxene compositions in terms of tetrahedral aluminium (Al_{IV}) atoms pfu versus Ti atoms pfu for (a) Petit St. Vincent xenoliths and lava, and (b) fractional crystallisation experiments of Ulmer et al. (2018) and Nandedkar et al. (2014). Symbols in (a) as in Figure 5. Numbers next to symbols in (b) are temperatures in ºC. Green and black arrows on (a) and (b) denote magmatic evolution trends.

Figure 7. Variation in amphibole compositions for Petit St. Vincent xenoliths in terms of (a) tetrahedral aluminium (Al_{IV}) atoms pfu versus Mg#; and (b) wt% Cl versus K_2O. Igneous xenoliths in filled red symbols; meta-igneous in open blue symbols with PSV10 and PSV17 distinguished. Decreasing Al_{IV} with increasing Mg# is indicative of cooling and oxidation in meta-igneous amphiboles. Unpublished data from Butt (2012) are included.

Figure 8. Major element variations in Petit St. Vincent lavas, igneous and meta-igneous xenoliths (calculated from mineral modes and compositions), and xenolith melt inclusions (MI – PEC-corrected). Xenoliths denoted as triangles; MI as coloured crosses; lavas as black diamonds. Grey symbols denote compositions of M-series and C-series lavas from Grenada and other southern Lesser Antilles arc lavas (St Vincent, Grenada, Grenadines) for comparison (GEOROC database and Camejo-Harry et al., 2018 and 2019). One standard deviation uncertainties on recalculated xenoliths whole-rock are fully propagated from uncertainties on mean mineral compositions and modal proportions.

Figure 9. Trace element concentrations in plagioclase from Petit St. Vincent lava and xenoliths plotted against Sr: (a) La; (b) Ba; (c) Li; and (d) Cu (one plagioclase phenocryst from lava contains 80 ppm Cu). Igneous xenoliths shown as orange symbols with Sr-rich plagioclases from PSV20 highlighted in red; meta-igneous xenolith in blue open symbols; phenocrysts from lava in black. Insets in (a) and (b) show whole-rock variation for C-series 'ankaramites' (red) and M-series 'picrites' (grey) from Grenada (Thirlwall et al., 1996; White et al., 2017), as well as Petit St. Vincent lavas. Corresponding differentiation trends are superimposed on the plagioclase data in (a). Cores and rims for some phenocryst and xenolith plagioclases are illustrated on (a). Note that plagioclase from PSV8 differs from plagioclase from other meta-igneous samples, resembling more closely igneous plagioclases.

Figure 10. Rare earth element patterns of clinopyroxene and amphibole from Petit St. Vincent xenolith and lava normalised to primitive mantle values (Palme and O'Neill 2003): (a) and (b) clinopyroxene from igneous (orange and red lines) and meta-igneous xenoliths (blue lines), respectively, compared to clinopyroxene from lava (green lines); (c) and (d) amphibole from igneous and meta-igneous xenoliths, respectively. Note the enrichment of LREE in PSV8 both in amphibole and clinopyroxene relative to the rest of meta-igneous xenoliths. REE depletion in amphibole rim from PSV3 is indicated in (c).

Figure 11. Chemistry of clinopyroxenes from Petit St. Vincent lava and xenoliths for selected trace elements plotted against Sr: (a) La, (b) Li, (c) Zr and (d) Ta. Symbols as in Figure 9. As for plagioclase, note Sr enrichment in clinopyroxene from PSV20. Aluminium-poor cores and Al-rich rims for some phenocryst and xenolith plagioclases are illustrated on (a). The increased range of concentration from La^{3+} to Zr^{4+} to Ta^{5+} in the igneous xenolith and lava clinopyroxenes is consistent with the known dependence of clinopyroxene-melt partition coefficients on cation charge.

Figure 12. Chemistry of amphiboles from Petit St. Vincent xenoliths for selected trace elements plotted against Sr: (a) Zr, (b) La, (c) Li and (d) Ba. Symbols as in Figure 9 except for lavas that lack amphibole. Note the extreme variation (factor ~100) in La (and other LREE) in meta-igneous amphiboles.

Figure 13. Textures and crystallographic fabrics of representative igneous (a-c) and meta-igneous (d-f) xenoliths. Igneous pyroxene-hornblende gabbro xenolith PSV11: (a) Photomicrograph in XPL of showing E-W aligned plagioclase; (b) same image in PPL showing interstitial amphibole and amphibole overgrowth on clinopyroxene; (c) contoured pole EBSD figures for the main mineral components showing concentrations in terms of multiples of uniform distribution. This sample shows no clear microstructural evidence for subsolidus deformation, but does display a clear magmatic layering that is oriented roughly

NE–SW, perpendicular to the concentration of poles to the (001) planes of plagioclase and clinopyroxene. The weaker fabric in amphibole reflects topotactic overgrowth on clinopyroxene. Images were taken from an area of ~15 x 22 mm. The number of indexed points, J-index and M-index for the three different minerals are: plagioclase (14608, 4.8392, 0.1100), clinopyroxene (5759, 3.9596, 0.0782) and amphibole (4122, 2.9435, 0.0308). Mylonitic meta-igneous xenolith PSV10: (d) photomicrograph in PPL showing domains of recrystallised plagioclases enveloped by microcrystalline clinopyroxene; (e) high-magnification photomicrograph in PPL displaying amphibole both filling pore-space between clinopyroxene grains and forming discrete oriented grains. Note triple junctions between plagioclase grains, suggestive of the former presence of intergranular fluid; (f) contoured pole figures for the main mineral components showing concentrations in terms of multiples of uniform distribution. The deformation-related foliation is oriented E–W. The grain size is much smaller than PSV11 and an imaged area of 700 x 500 μm was sufficient to obtain a representative result. The number of indexed points, J-index and M-index are: plagioclase (90211, 1.6168, 0.0091), clinopyroxene (89026, 1.7238, 0.0142) and amphibole (51404, 1.4015, 0.0102).

Figure 14. Averaged, PUM-normalised trace element patterns for melts calculated to be in equilibrium with amphiboles in five igneous xenoliths (PSV3, PSV12, PSV14, PSV19, PSV20) using method described in text. Error bars are 1 sd of the mean. Note remarkable match between calculated trace element patterns and trachyandesite (PM2b) and dacite (PM2a) lavas from the adjacent island of Petite Martinique. Distinctive chemistry of a Grenada andesite (GR5) shown for comparison. Whole-rock data from Rojas-Agramonte et al. (2017). Uranium and Th highlighted for clarity.

Figure 15. Modelled and observed behaviour of (a) Th-U and (b) Sr-Y in amphibole during incongruent, fluid-fluxed partial melting of clinopyroxene and plagioclase at three representative temperatures (grey and black lines). Igneous xenoliths shown in red, meta-igneous in blue, with individual xenoliths PSV20 and PSV8 highlighted for clarity. Melting progressively depletes amphiboles in Th and Y and modifies Th/U and Sr/Y ratios. The offset between the Sr/Y ratios of igneous and meta-igneous amphiboles in (b) reflects different source lithologies, with PSV8 having intermediate characteristics. Tick marks on model curves denote 2% increments in degree of melting from 0 to 18%. See text for description of the method. Error bars denote fully propagated analytical uncertainties. All concentration normalised to PUM.

Figure 16. Extended, PUM-normalised trace element patterns produced by incongruent partial melting of clinopyroxene and plagioclase according to Reaction (6) for (a) igneous xenolith amphiboles and (b) meta-igneous xenolith amphiboles. Starting (enriched) amphibole composition for melting models shown as solid black lines; selected depleted amphiboles shown as black dashed lines. Model calculations shown as coloured lines denote 5% melting (F=0.05) at 970 °C and 18% (0.18) melting at 850 °C for igneous xenoliths in (a) and 10% melting (0.10) at 800 °C and 5% (0.05) melting at 800 °C for meta-igneous xenoliths in (b). Note low degree of melting required to generate positive Sr anomaly in igneous amphibole (PSV20, PSV3). Strontium, U and Th highlighted for clarity.

Figure 17. Numerical simulation of sequential basalt sill emplacement into 10 km-thick sub-arc crust. One 300 m sill was emplaced randomly every 60 kyr between 8 and 12 km depth. (a) Initial temperature profile. (b-d) Conditions after 3.8 Myr of sill emplacement and crustal thickening by 19 km. Sills are shaded grey. Location of partially-melted screens of crust is a consequence of the random emplacement scheme. (b) Temperature profile. (c) Melt fraction for the case an amphibolite crust undergoing dehydration melting. (d) Melt fraction for the

case of a basaltic crust with 4.5 wt% of H_2O, simulating H_2O-fluxed melting. Note the greater crustal melt fraction (red lines) in (d) compared to (c), although most melt is generated through crystallisation of the basalt sills themselves (blue dashed lines).

Supplementary Figures

Figure A1. Variation in spinel composition for Petit St. Variation xenoliths and lava in terms of (a) Ti atoms per formula unit; (b) Cr# (100Cr/(Cr + Al)); (c) Fe^{3+}# (100Fe^{3+}/(Fe^{3+} + Cr + Al)); (f) Al# (100Al/(Al + Fe^{3+} + Cr)) versus Mg# (Mg/(Mg+Fe^{2+})). Legend same as Figure 6.

Figure A2. Extended PUM-normalised trace element patterns for (a) igneous and (b) meta-igneous xenolith clinopyroxenes.

Figure A3. Extended PUM-normalised trace elements patterns for (a) igneous and (b) meta-igneous xenolith amphiboles.

Figure A4. Calculated amphibole-melt partition coefficients ($D_{amph/L}$) used in modelling, calculated for a representative D_{Ca} = 1.7. Values calculated according to method described in text using data from Nandedkar et al. (2016). Error bars denote 1 sd uncertainties; large uncertainties for Pb, U and Th discussed in the text.

Figure A5. Melt function versus temperature (*F*-*T*) relationship used in the numerical simulation of sill emplacement for amphibolite (at two different pressures) and hydrous basalt crust. The injected basalt has the same *F*-*T* relationship as the hydrous basalt.

Fig. 1.

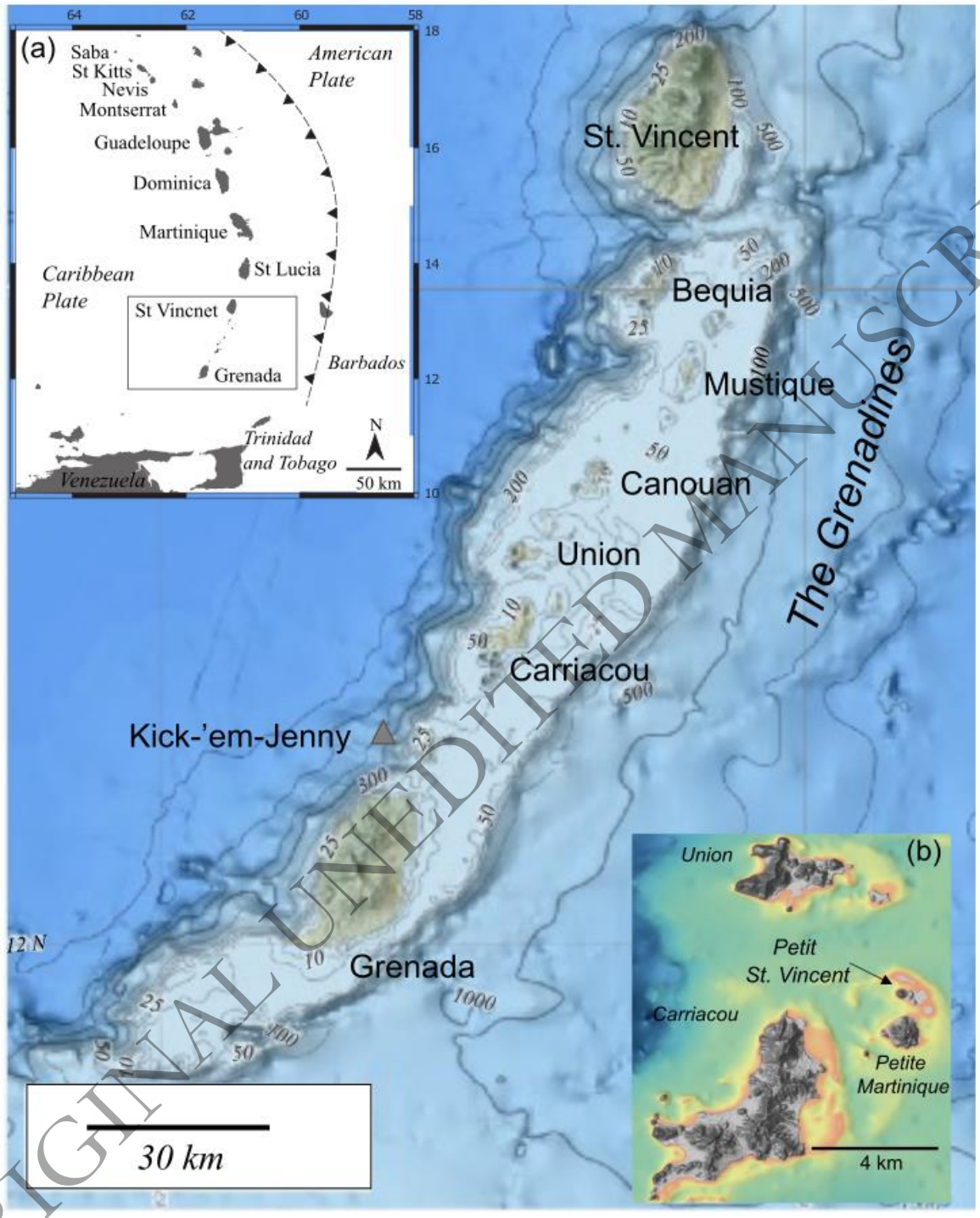

Fig. 2.

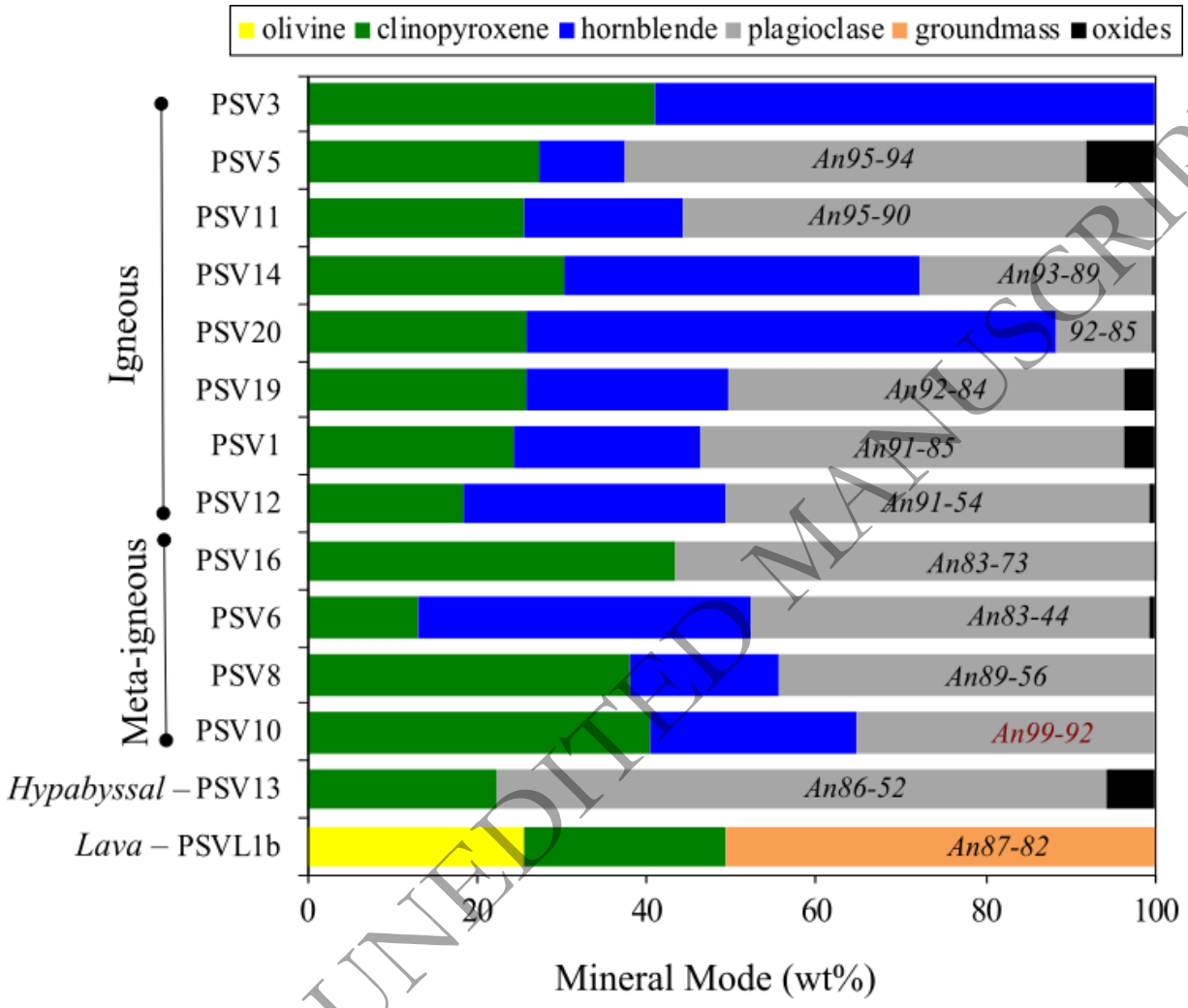

Fig. 3.

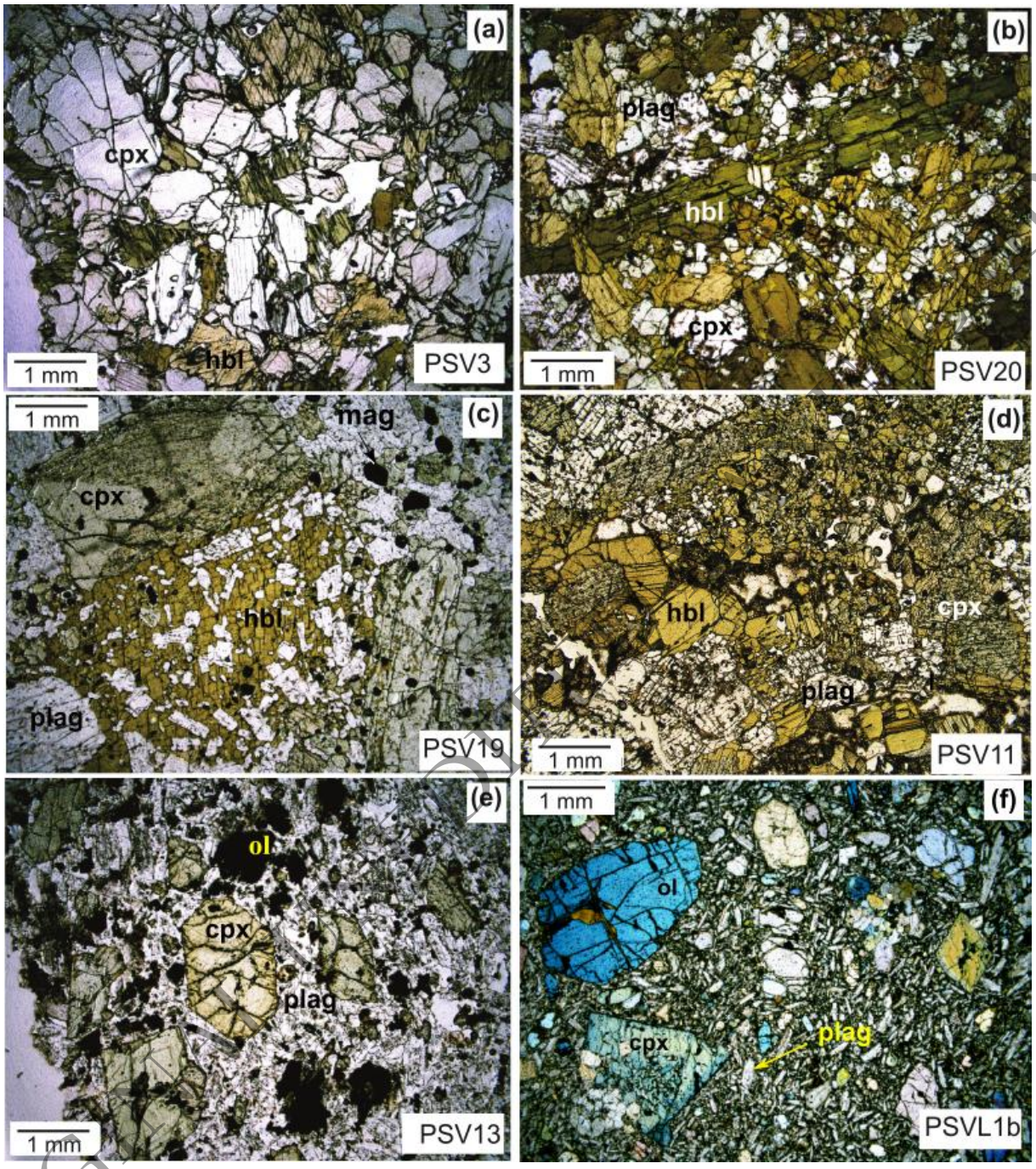

Fig. 4.

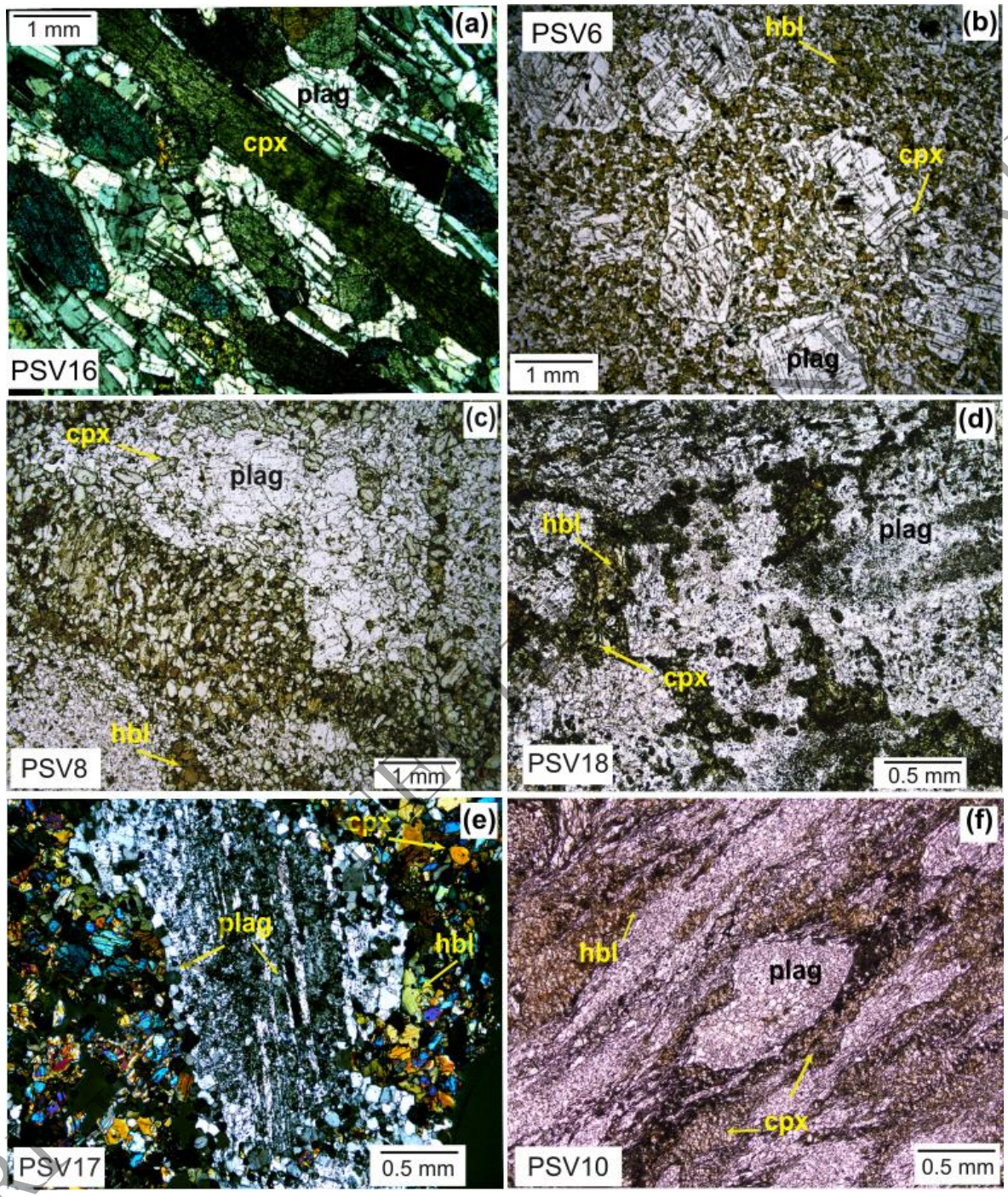

Fig. 5.

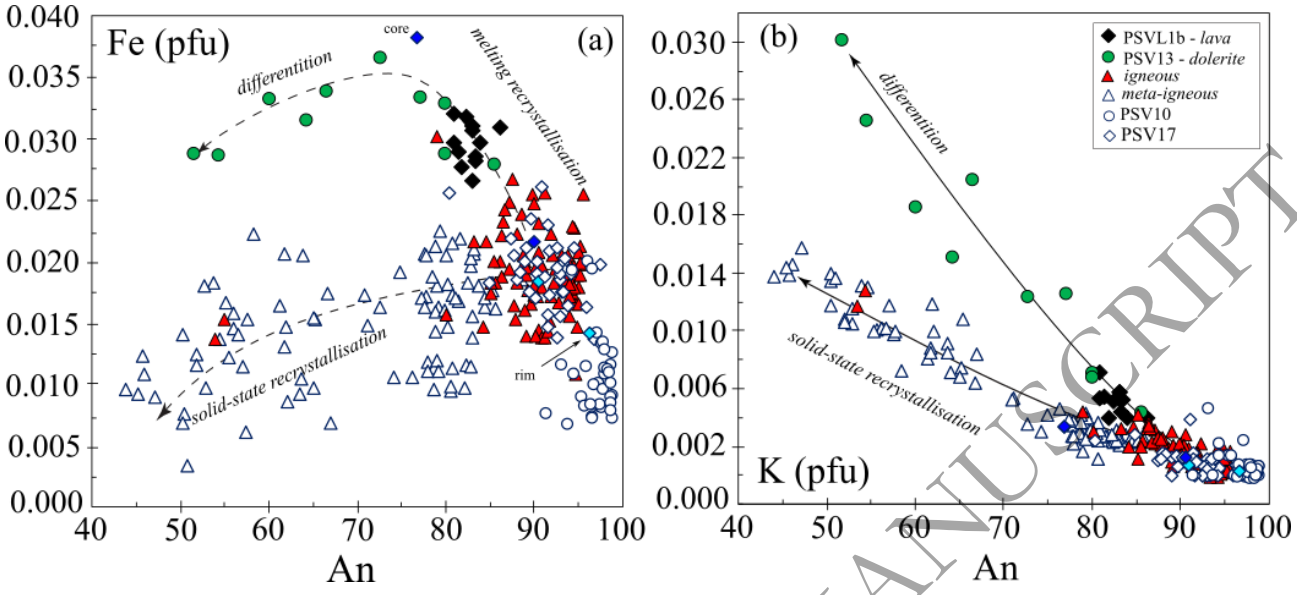

Fig. 6.

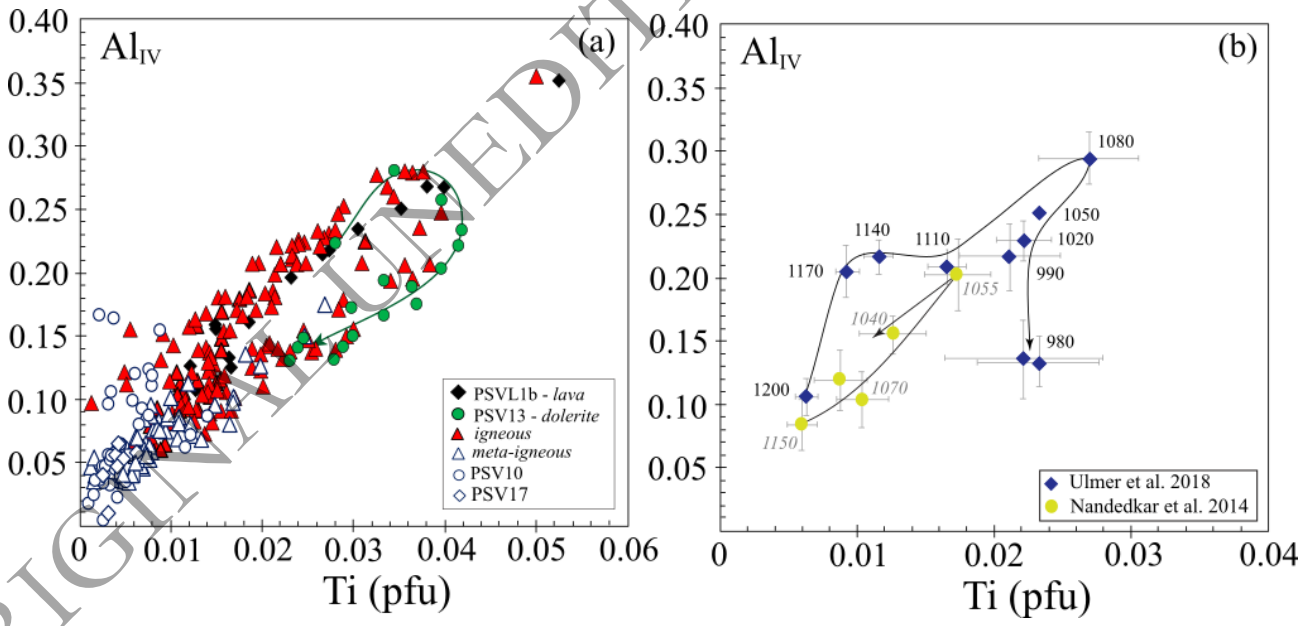

Fig. 7.

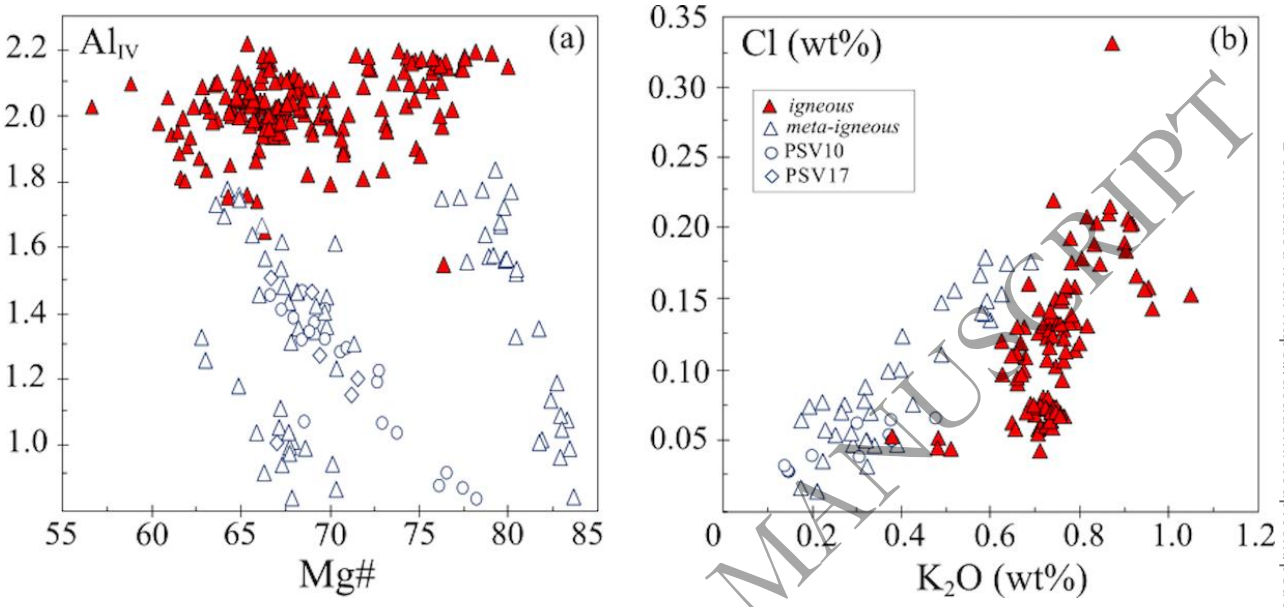

Fig. 8.

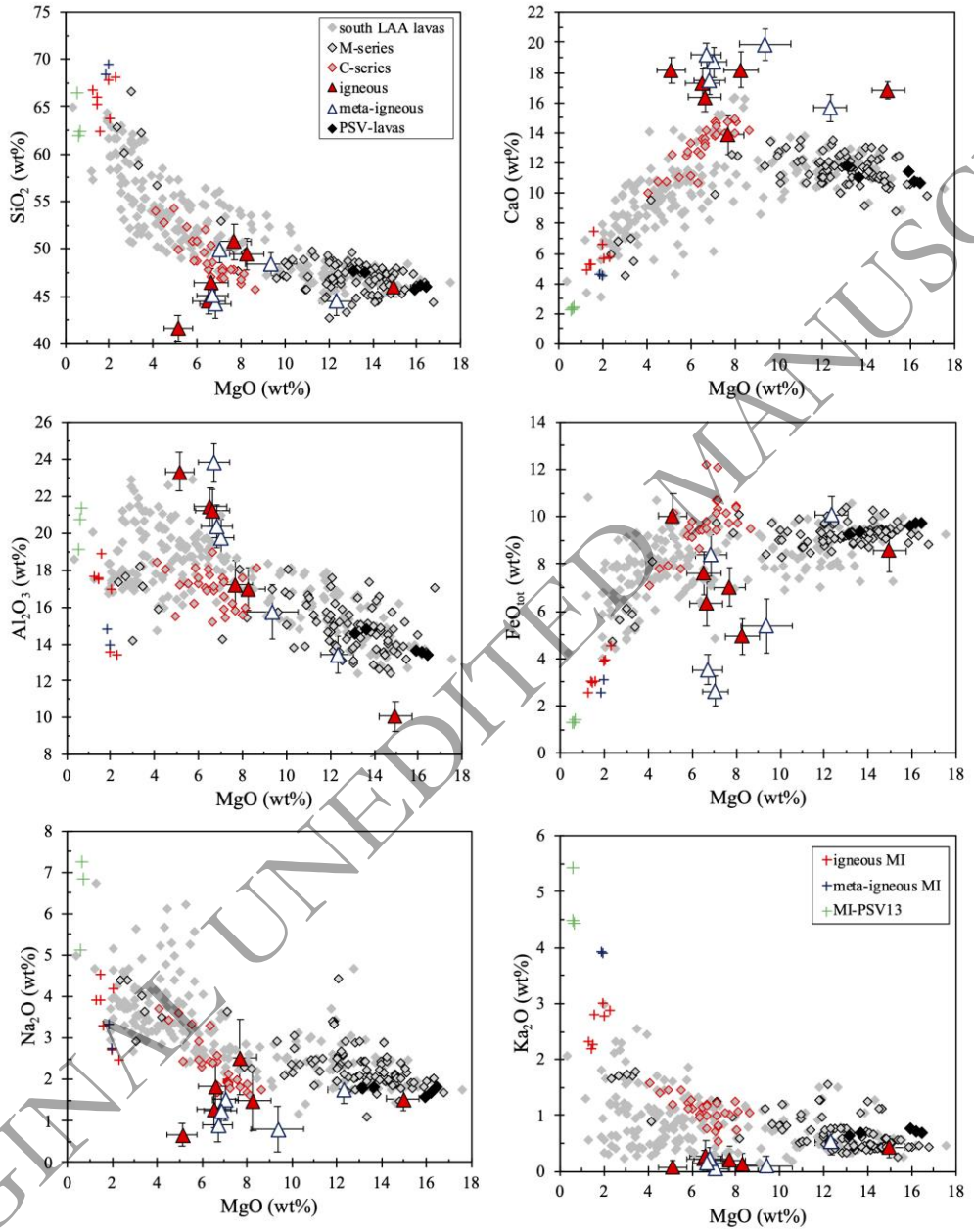

Fig. 9.

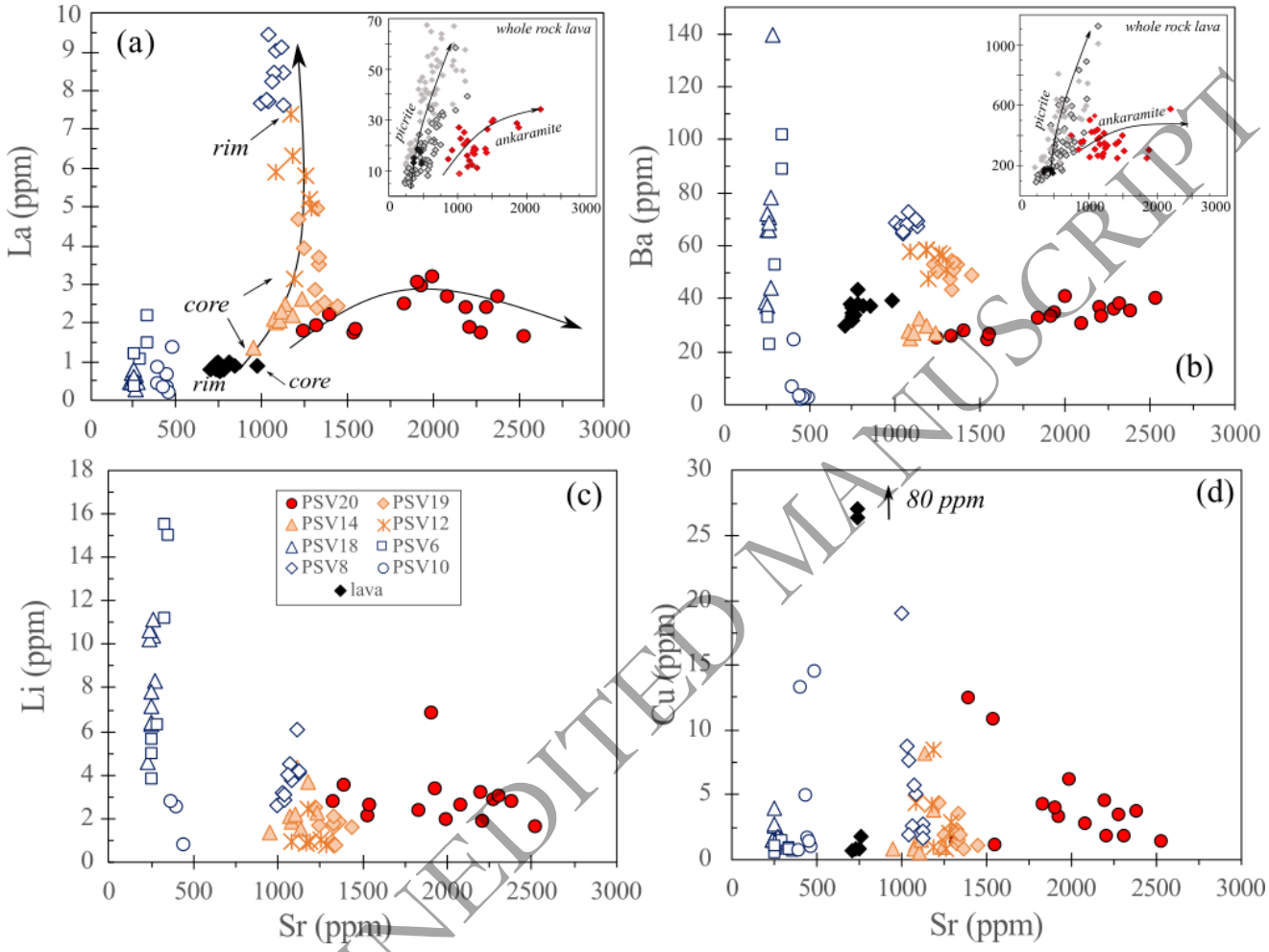

Fig. 10.

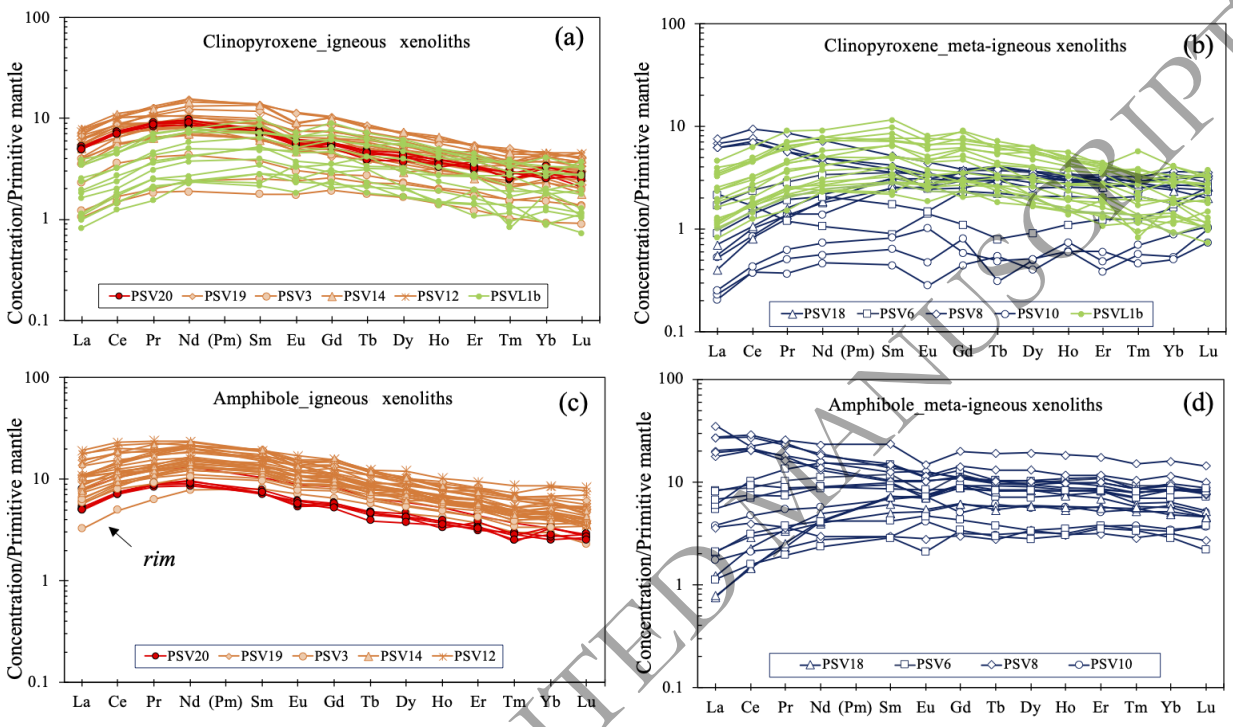

Fig. 11.

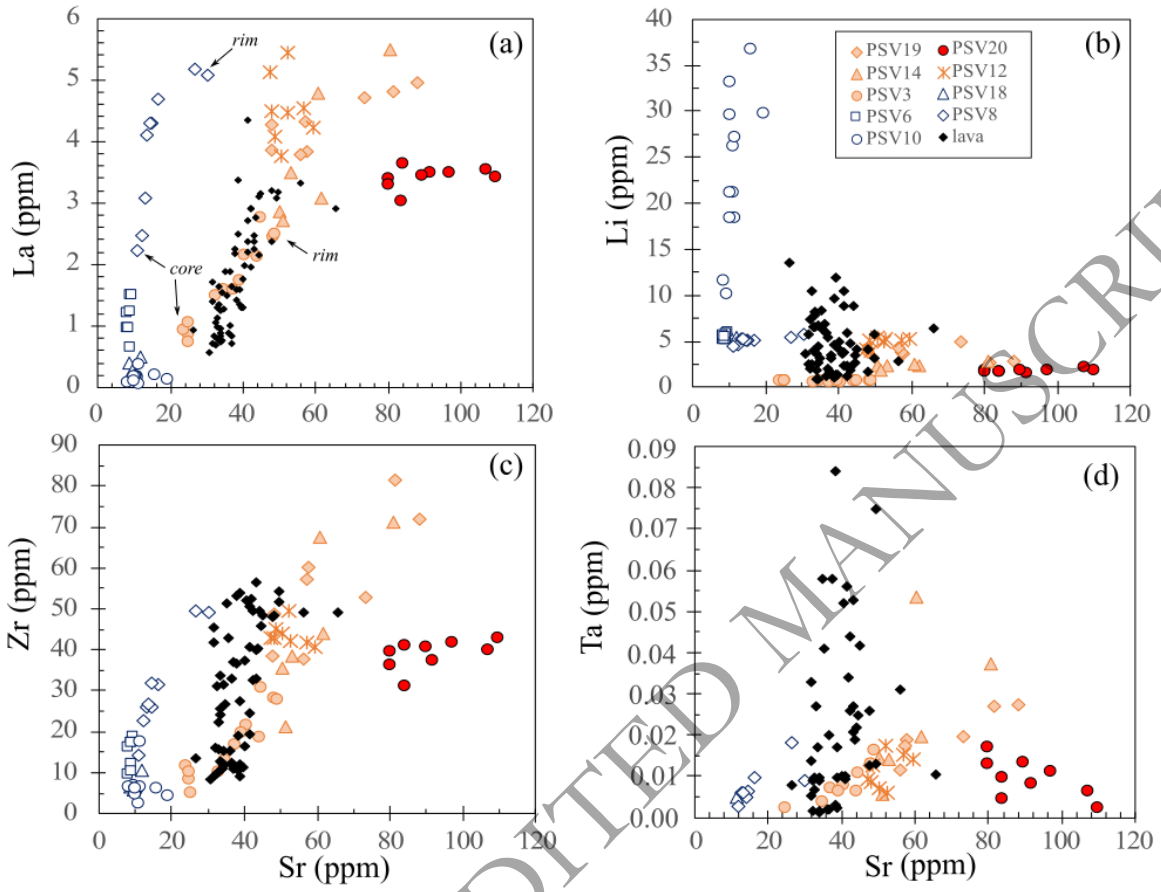

Fig. 12.

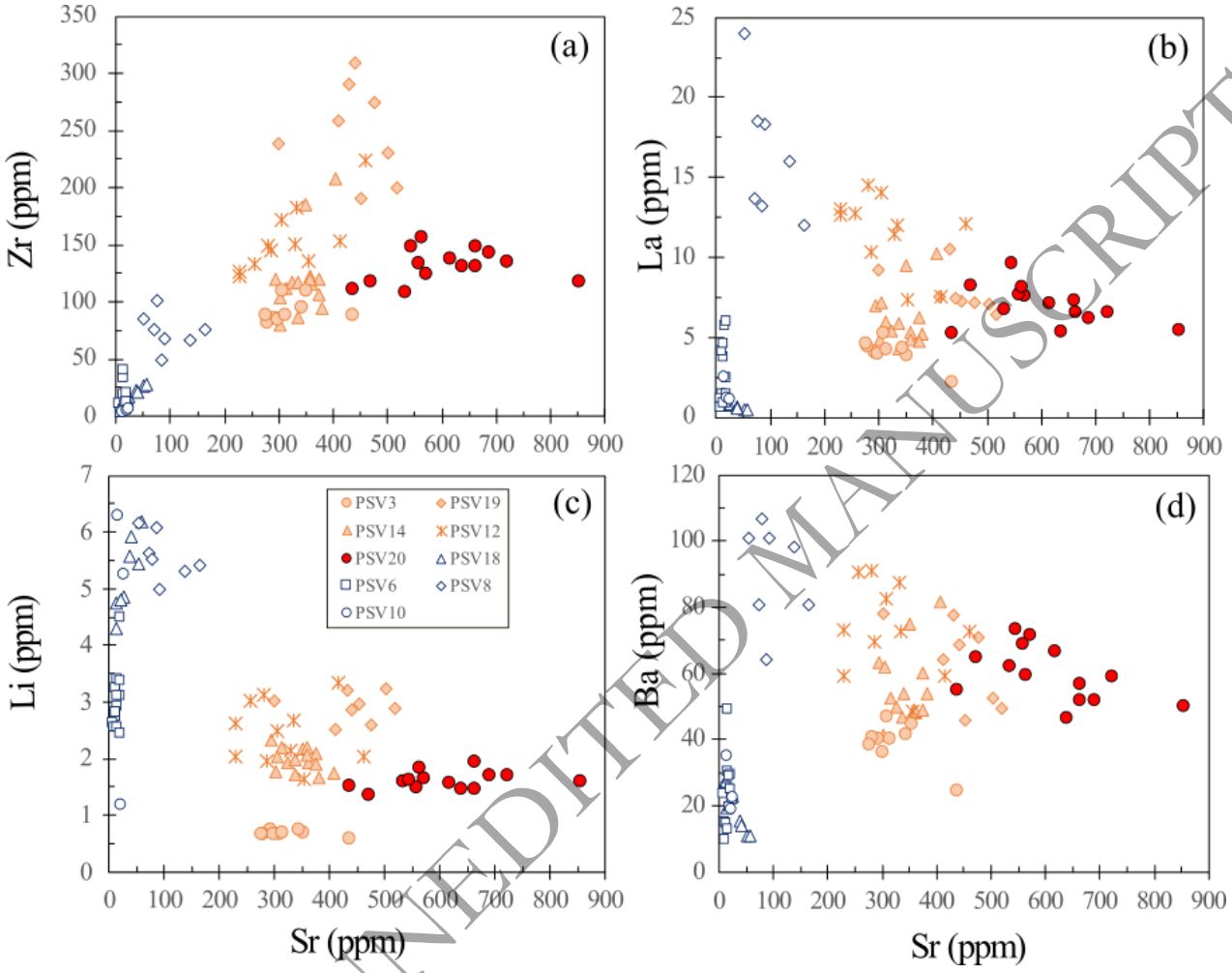

Fig. 13. (a,b,c)

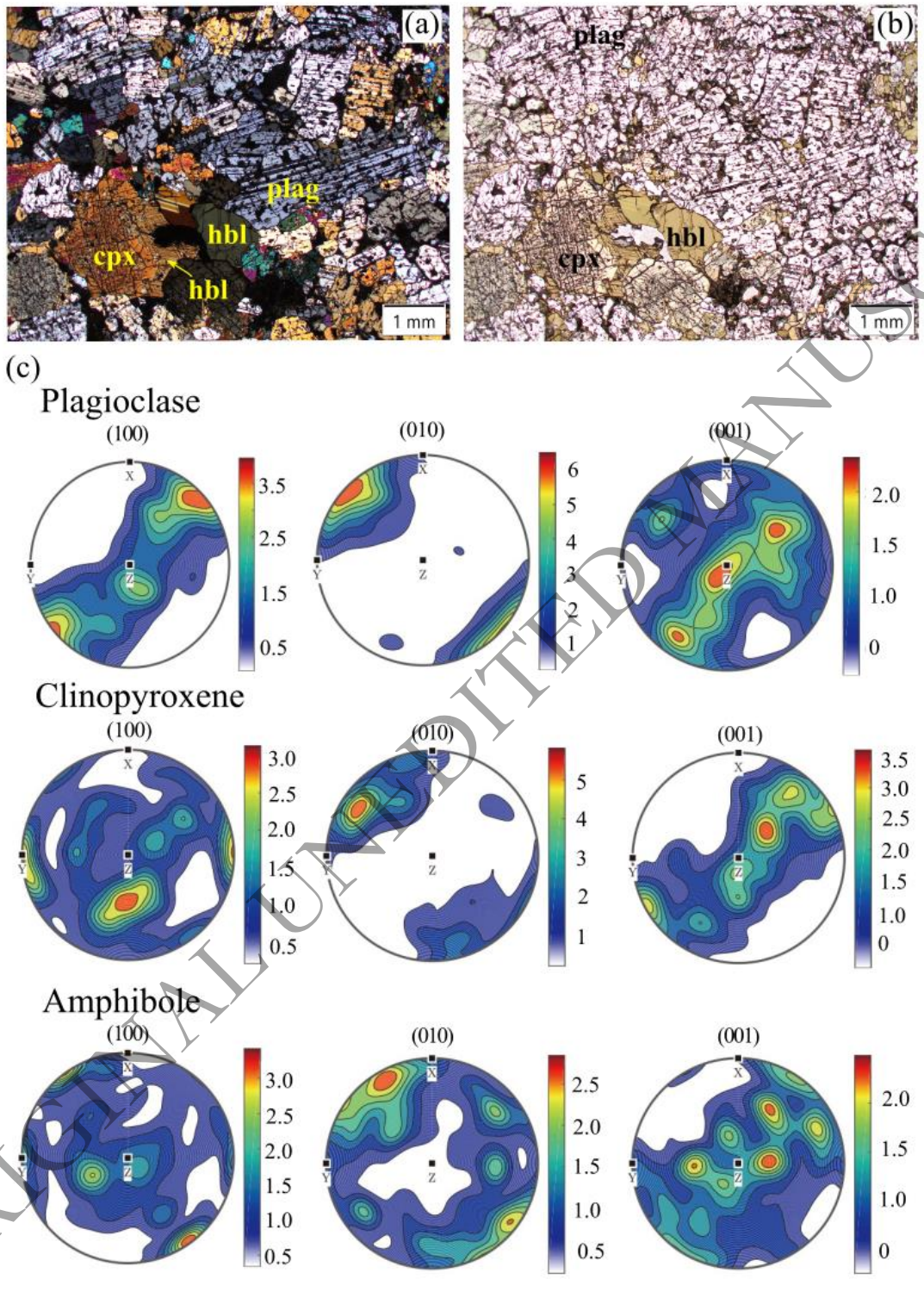

Fig. 13. (d,e,f)

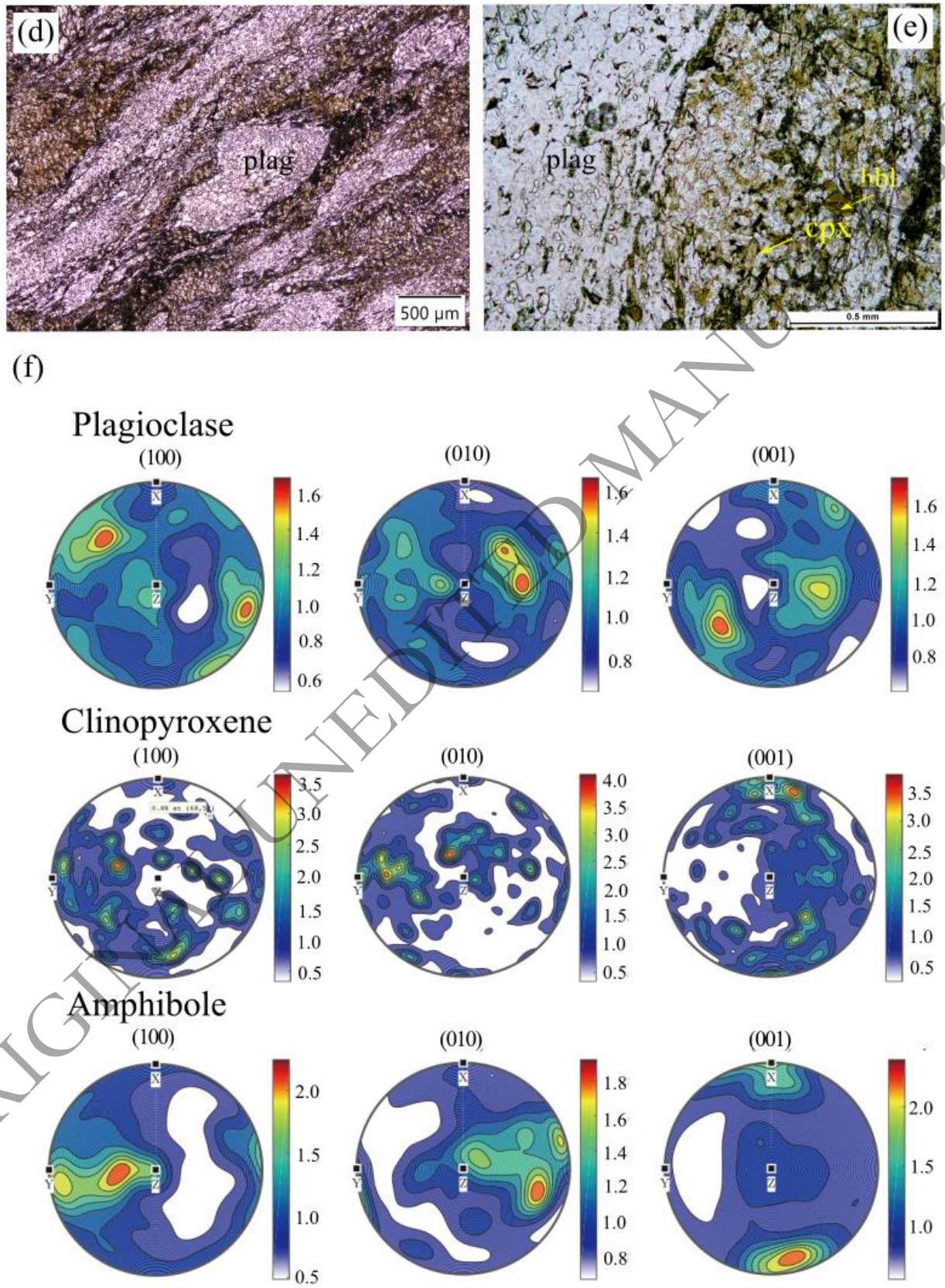

Fig. 14.

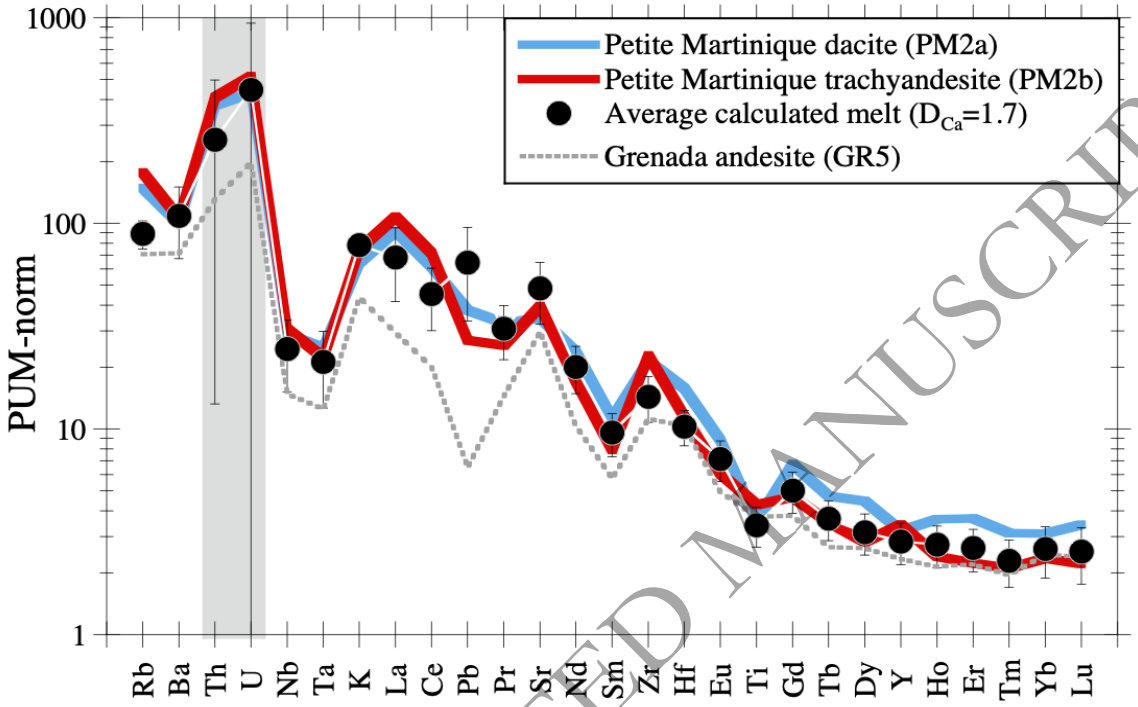

Fig. 15. (a)

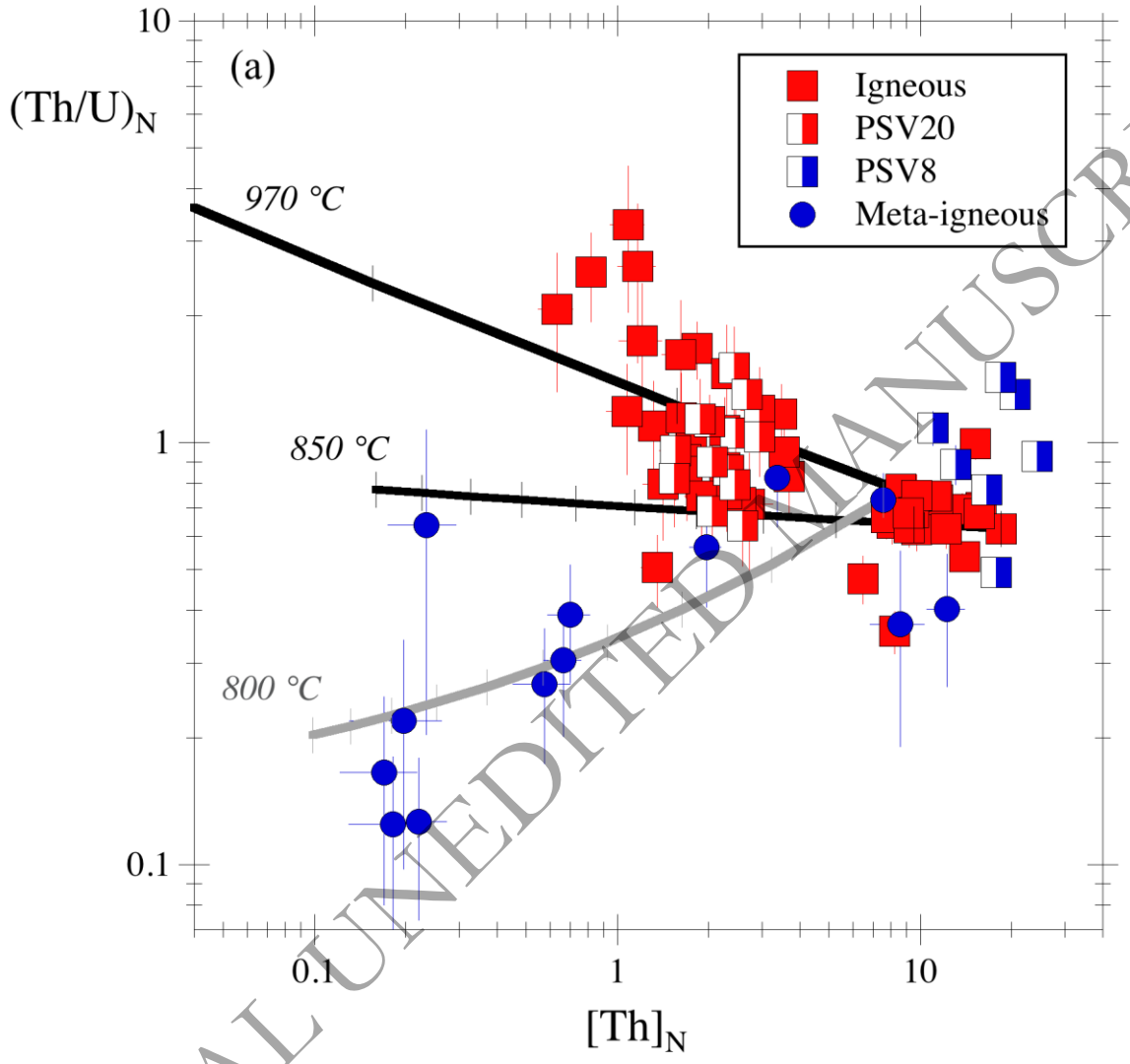

Fig. 15. (b)

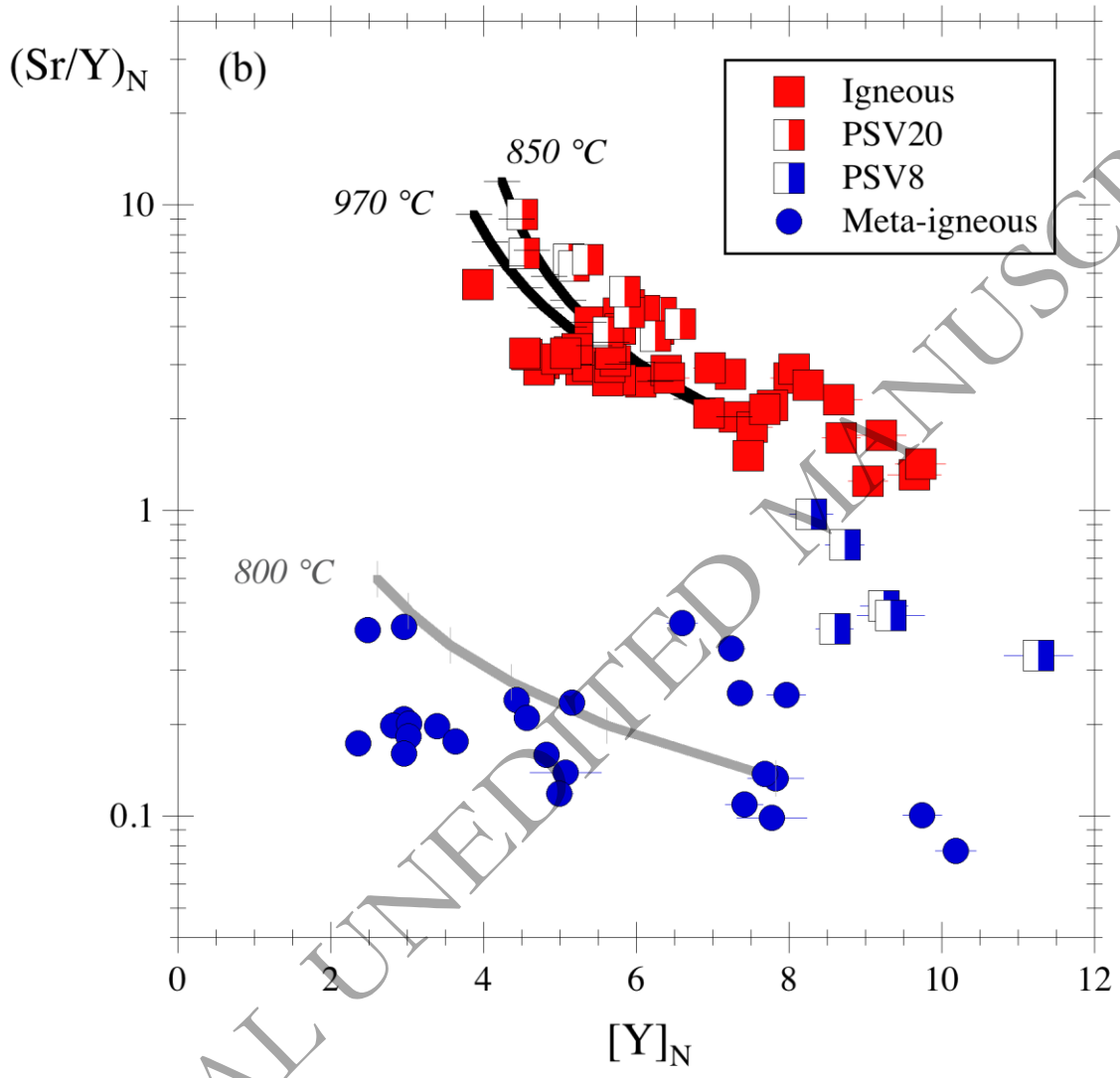

Fig. 16.

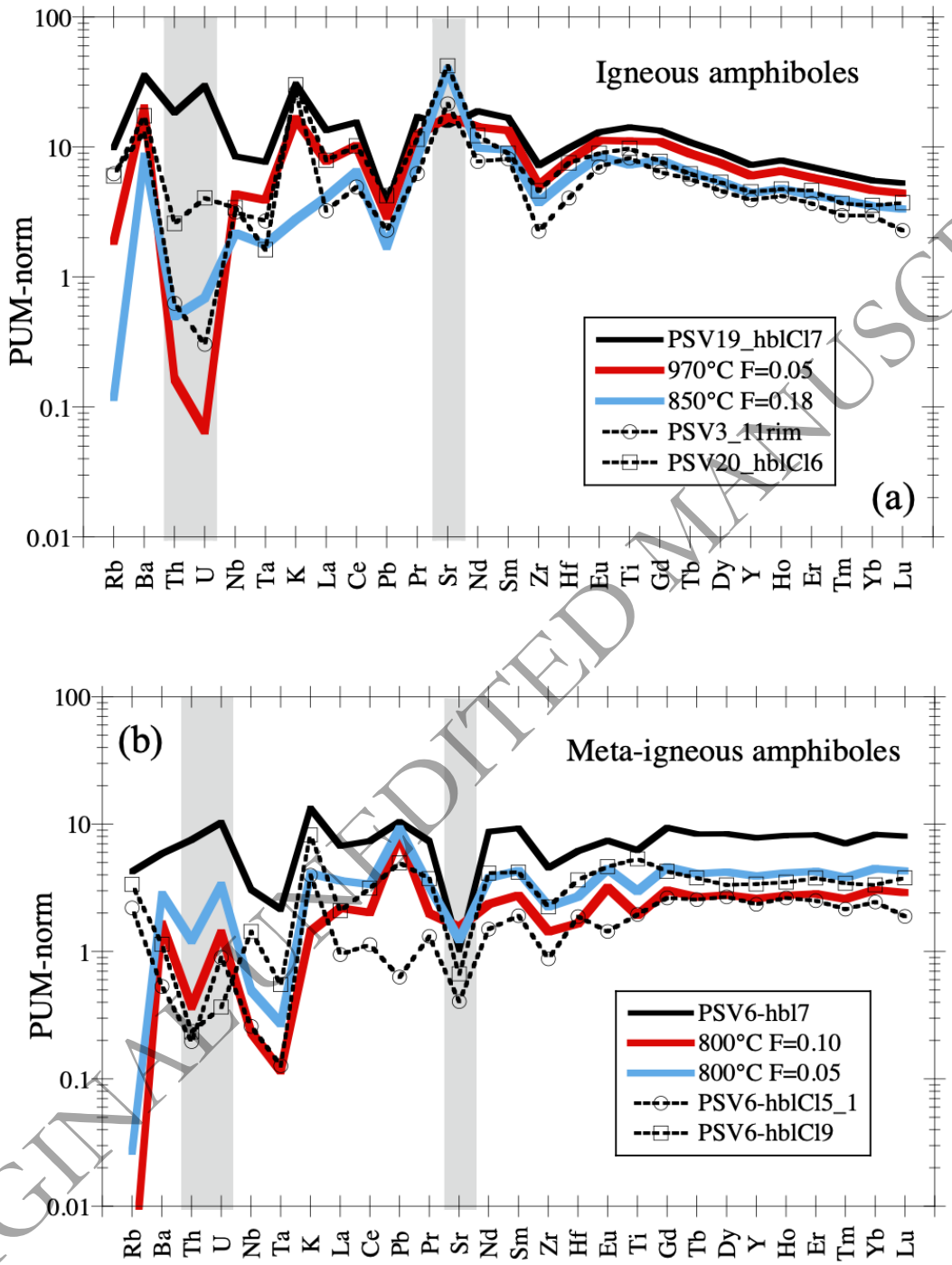

Fig. 17.